JCI The Journal of Clinical Investigation

Epsilon toxin-producing *Clostridium perfringens* colonize the MS gut and epsilon toxin overcomes immune privilege

Yinghua Ma, … , Christopher E. Mason, Timothy Vartanian

J Clin Invest. 2023. https://doi.org/10.1172/JCI163239.

Research In-Press Preview **Autoimmunity** **Microbiology**

Graphical abstract

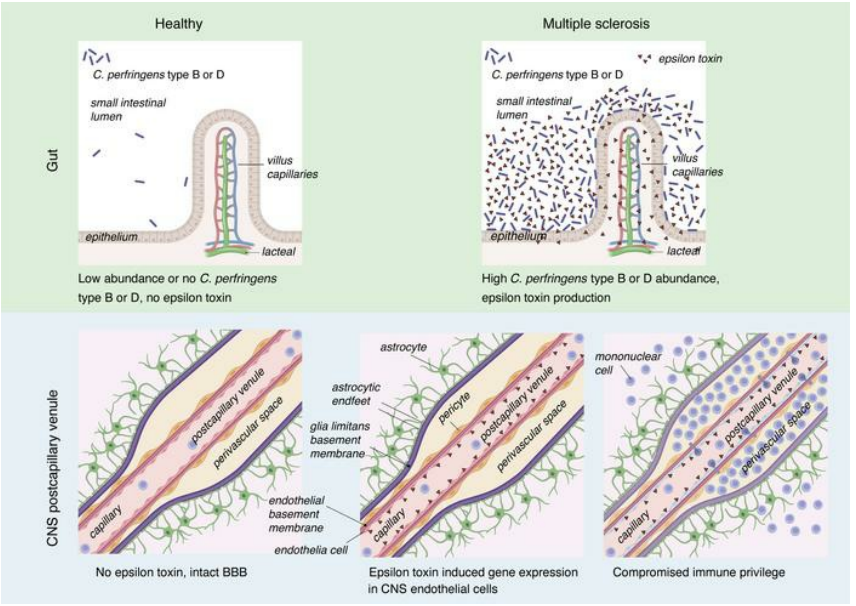

Find the latest version:

https://jci.me/163239/pdf

Epsilon Toxin-Producing *Clostridium perfringens* colonize the MS Gut and Epsilon Toxin Overcomes Immune Privilege

Yinghua Ma[1]*, David Sannino[1]*, Jennifer R. Linden[1]*, Sylvia Haigh[1], Baohua Zhao[1], John B. Grigg[2,3,4,5], Paul Zumbo[6,7], Friederike Dündar[6,7], Daniel Butler[7], Caterina P. Profaci[8], Kiel Telesford[1], Paige Winokur[9], Kareem Rashid Rumah[10], Susan Gauthier[11], Vincent A. Fischetti[10], Bruce A. McClane[12], Francisco A. Uzal[13], Lily Zexter[11], Michael Mazzucco[1], Richard Rudick[14], David Danko[7], Evan Balmuth[1], Nancy Nealon[11], Jai Perumal[11], Ulrike Kaunzner[11], Ilana L. Brito[15], Zhengming Chen[16], Jenny Z. Xiang[17], Doron Betel[6,7], Richard Daneman[8], Gregory F. Sonnenberg[2,3,4,5], Christopher Mason[7]✉, and Timothy Vartanian[1,5,11,18]✉

1. Feil Family Brain and Mind Research Institute, Weill Cornell Medical College, Cornell University, New York, NY, USA

2. Jill Roberts Institute for Research in Inflammatory Bowel Disease, Weill Cornell Medical College, Cornell University, New York, NY, USA

3. Joan and Sanford I. Weill Department of Medicine, Weill Cornell Medical College, Cornell University, New York, NY, USA

4. Department of Microbiology and Immunology, Weill Cornell Medical College, Cornell University, New York, NY, USA

5. Immunology and Microbial Pathogenesis Program, Weill Cornell Medicine, New York, NY, USA

6. Applied Bioinformatics Core, Division of Hematology/Oncology, Department of Medicine, Institute for Computational Biomedicine, Weill Cornell Medicine, New York, NY, USA

7. Physiology and Biophysics, Institute for Computational Biomedicine, Weill Cornell Medical College, Cornell University, USA

8. Departments of Pharmacology and Neurosciences, University of California, San Diego, CA, USA

9. Harold and Margaret Milliken Hatch Laboratory of Neuro-endocrinology, Rockefeller University, New York, NY, USA

10. Laboratory of Bacterial Pathogenesis and Immunology, Rockefeller University, New York, NY, USA

11. Department of Neurology, Weill Cornell Medical College, Cornell University, New York, NY, USA

12. Department of Microbiology and Molecular Genetics, University of Pittsburgh School of Medicine, Pittsburgh, Pennsylvania, USA

13. California Animal Health and Food Safety Laboratory, School of Veterinary Medicine, University of California, Davis, California, USA

14. Astoria Biologica Inc, Norwalk, CT, USA

15. Meinig School of Biomedical Engineering, Cornell University, Ithaca, USA

16. Division of Biostatistics, Department of Population Health Sciences, Weill Cornell Medicine, New York, NY, USA

17. Genomics Resources Core Facility, Core Laboratories Center, Weill Cornell Medicine, New York, NY, USA

18. Lead Contact

*These authors contributed equally to the work.

✉ e-mail: tiv2002@med.cornell.edu; or, chm2042@med.cornell.edu;

Timothy Vartanian MD, PhD, Weill Cornell Medical College, Cornell University, 1305 York Avenue, New York, NY 10021

Abstract

Multiple Sclerosis (MS) is a complex disease of the CNS thought to require an environmental trigger. Gut dysbiosis is common in MS, but specifically causative species are unknown. To address this knowledge gap, we used sensitive and quantitative PCR detection to show that people with MS were more likely to harbor and show a greater abundance of epsilon toxin (ETX)-producing strains of *C. perfringens* within their gut microbiomes compared to healthy controls (HC). MS patient-derived isolates produced functional ETX and had a genetic architecture typical of highly conjugative plasmids. In the active immunization model of experimental autoimmune encephalomyelitis (EAE), where pertussis toxin (PTX) is used to overcome CNS immune privilege, ETX can substitute for PTX. In contrast to PTX-induced EAE, where inflammatory demyelination is largely restricted to the spinal cord, ETX-induced EAE caused demyelination in the corpus callosum, thalamus, cerebellum, brainstem, and spinal cord, more akin to the neuroanatomical lesion distribution in MS. CNS endothelial cell transcriptional profiles revealed ETX-induced genes that are known to play a role in overcoming CNS immune privilege. Together, these findings suggest that ETX-producing *C. perfringens* strains are biologically plausible pathogens in MS that trigger inflammatory demyelination in the context of circulating myelin autoreactive lymphocytes.

Introduction

MS lesions are centered on post-capillary venules (1, 2), and impairment of blood-brain barrier (BBB) function is considered the earliest event in lesion evolution, paving the way for entry of myelin autoreactive lymphocytes (2-4). MS disease initiation, and thus lesion formation, is believed to require an environmental trigger in a genetically susceptible individual, but biologically plausible environmental agents responsible for lesion induction have been elusive (5, 6). Recent studies have consistently identified dysbiosis in MS patients, based on taxonomic and functional features of the gut microbiome (7-19). Transfer of gut microbiota from identical twins discordant for MS revealed a significantly higher incidence of autoimmunity in mice receiving microbiota from MS-affected compared to healthy twins (9). Several studies in mice provide compelling evidence that the MS gut microbiome harbors microbes that directly act on adaptive immune cells to enhance or suppress autoimmunity (9, 12, 20-25). *C. perfringens* ETX is a unique candidate environmental trigger for MS because this bloodborne neurotoxin specifically targets CNS endothelial cells, leading to disruption of BBB integrity (26).

C. perfringens is a gram-positive anaerobe categorized into 7 toxinotypes based on production of one or more of 6 major toxins (27). The type B and D strains carry the plasmid-encoded ETX gene (*etx*) (27). In the gastrointestinal tract of mammals, *C. perfringens* types B and D exist in the small intestine where they produce ETX episodically during log-phase growth (28-30). Human exposure to *C. perfringens* strains is broad since they are present in our food chain, pets, and are found in multiple ecological niches including farm runoff, sewage, marine sediment, soil, and the gastrointestinal tracts of fish, birds, and mammals (31-43). As a spore-forming anaerobe, once

C. perfringens enters an environment it tends to persist due to resistance of spores to heat, chemicals, radiation, and pressure (44-46). Following environmental exposure and oral ingestion, colonization of the small intestine is thought to be dependent on host genetics, microbiome composition, and additional factors such as prior antibiotic use (47).

ETX is a member of the aerolysin-family of pore-forming toxins (48-50). ETX is synthesized as a 32.9 kDa inactive pro-toxin that is cleaved in the gut by host serine proteases and carboxypeptidases (48, 51) or occasionally by bacterially-derived lambda protease into a 27 kDa active toxin (48, 52). The ETX monomer crosses the small intestine without causing injury or enteritis (53). We identified the myelin and lymphocyte protein (MAL) as the receptor for ETX (54), required for binding and for all known biologic activity (26, 54-58). MAL is localized to lipid rafts and ETX binding to MAL brings monomers in proximity, favoring self-assembly into a heptameric pre-pore complex that then inserts into the plasma membrane of host cells (59-61). In the bloodstream, ETX has access to all vascularized tissues, but its binding is restricted to CNS endothelial cells, since they are enriched for expression of the ETX receptor, MAL (26). In vivo, ETX induces BBB permeability (26, 56, 62-64).

In this report, we present evidence that ETX-producing strains of *C. perfringens* can function as environmental triggers for MS. To characterize the possible role of ETX in MS, we 1) identify an association between ETX-producing strains of *C. perfringens* and MS in clinical samples, 2) find that people with MS have increased abundance of ETX-producing strains of *C. perfringens* in their gut microbiome compared to healthy controls, 3) show that ETX is sufficient to induce multifocal,

inflammatory demyelination in the context of active immunization with MOG_{35-55}, 4) demonstrate that ETX-induced inflammatory demyelination, in active EAE, more closely resembles the lesion distribution observed in MS when compared to the traditional PTX model, and 5) find that, in CNS endothelial cells, ETX induces expression of genes known to overcome CNS immune privilege.

Results

The MS gut microbiome harbors ETX-producing C. perfringens strains.

Based on a statistical power calculation (Methods), 62 participants were recruited under the IRB protocol: Harboring the Initial Trigger of Multiple Sclerosis (HITMS), consented, and received instruction on self-collection of fecal samples. Healthy controls (HC) and MS participants were matched for age, gender, body-mass index, location of residence at time of fecal sample donation, and ancestry/ethnicity (Supplemental Table 1, Supplemental Figure 1). Inclusion into the MS arm required a diagnosis of confirmed MS based on the 2010 revised McDonald criteria (65). Participants having a 1st or 2nd degree relative with a diagnosis of MS, or a clinically isolated syndrome were excluded from the HC arm. Full inclusion and exclusion criteria are detailed in the Methods and Supplemental Methods.

We recognized that ETX-producing strains of *C. perfringens* would likely be in relative low abundance in human fecal samples based on the results of previous surveys (57, 66) and because the ecological niche of these mucosal-adherent bacteria is in the small intestine (67), a site known to be vastly underrepresented in fecal samples (68, 69). Low abundance in fecal samples likely

renders *C. perfringens* types B or D undetectable by metagenomics sequencing commonly utilized in MS microbiome studies (9, 12). We therefore utilized PCR, a more sensitive approach for gene detection than shot-gun metagenomics, to examine whether the *etx* gene is present in human gut microbiota. We used density gradient centrifugation, Nycodenz, in our study because separation of bacteria from non-microbial fecal matter removes PCR inhibitors, provides a more accurate representation of bacterial composition, and enhances recovery of the Phylum Bacillota (Firmicutes), and in particular the Class Clostridia (70) (Figure 1A). Our initial screen detected an occurrence of *etx* in 61% of MS patients and 13% of controls (Figure 1B). To confirm *etx*-positive study participants, we conducted an independent PCR, targeting a different region of the *etx* gene (Figure 1C). The identities of all PCR products were verified by Sanger sequencing. The *cpa/plc* gene, common to all *C. perfringens* strains, and the 16S ribosomal RNA gene specific to *C. perfringens,* were also detected in those *etx*-positive participants (Figure 1C), as anticipated, since only *C. perfringens* are known to naturally encode the *etx* gene. A Fisher's exact test of independence showed that *etx* is significantly associated with disease status (MS vs. HC) with $p = 0.0002$ (Figure 1D). The odds ratio of *etx*-positivity, MS vs HC, is 10.7, 95% CI: 2.9871 to 38.2381, $p = 0.0003$. We further conducted a multivariable logistic regression with *etx*- or *etx*+ status as a binary outcome to determine if disease status (MS vs. HC) as a whole or stratified by disease modifying treatment is associated with *etx* status, independent of sex. We found that the disease status was independently associated with *etx* status, even when adjusting for sex. In addition, the disease status (MS vs. HC), with or without treatment, was independently associated with *etx* status, adjusting for sex (Supplemental Table 2).

The prevalence of fecal *etx* positivity in our analysis is consistent with a previously reported frequency of ETX immunoreactivity in sera from people with clinically definite MS (43%) and age-matched controls (16%) (71). This suggests a high translation rate of the *C. perfringens* type B/D virulence factor, *etx*, and that the human gastrointestinal tract is a suitable environment for *C. perfringens* types B/D growth.

We next assessed the relative abundance of *etx* in fecal microbiota harvested from people with MS and HC. To do this, we performed quantitative analysis of *etx* abundance relative to universal *16S* by TaqMan real-time PCR using a modified $2^{-\Delta Ct}$ method (72). The $2^{-\Delta Ct}$ method allows normalization of real-time, quantitative PCR data to an internal reference. We assessed the abundance of *etx* relative to universal *16S* in MS and HC and found that *etx* abundance is significantly increased in fecal microbiota harvested from people with MS compared to HC (Figure 2, A and B).

C. perfringens type A strains, defined by presence of the chromosomally encoded alpha toxin gene, *cpa*, but none of the other major toxin genes, are human intestinal commensals (27, 73). *C. perfringens* type B strains carry the *cpa*, *cpb*, and *etx* toxin genes, whereas *C. perfringens* type D strains carry the *cpa* and *etx* genes (27). Our PCR analysis identified *cpa* in 74% of MS patients compared to 45% of controls (Supplemental Figure 2, A-C). When *cpa* prevalence was analyzed in subgroups of participants, according to the presence or absence of *etx*, *cpa* is coexistent with the *etx* gene in *etx*+ participants (Supplemental Figure 2D). Interestingly, *cpa* prevalence among *etx*-negative participants is essentially indistinguishable between people with MS and HC

(Supplemental Figure 2D). These results suggest non-*etx* strains (*cpa*+, *etx*-) are unlikely to be involved in MS. TaqMan real-time PCR showed a significant increase in *cpa* abundance for MS compared to controls (Figure 2C). No statistical difference for *cpa* abundance was found among subgroups according to *etx* presence/absence (Figure 2, D and E). Neither prevalence nor abundance of *cpa* from *etx*-negative participants differed between MS and HC, ruling out a role for non-*etx* strains in MS pathogenesis. However, an increase in *cpa* prevalence in the MS group (*etx*- and *etx*+ combined) compared to HC (Figure 2C) suggests that people with MS may have a more suitable gastrointestinal environment for the survival and growth of *C. perfringens*.

Quantification by TaqMan real-time PCR simultaneously targeting genes encoding *C. perfringens*-specific 16S rRNA and universal 16S rRNA confirmed an increase of *C. perfringens* abundance in MS compared to controls (Supplemental Figure 3A). Using the $2^{-\Delta\Delta Ct}$ method (72) with pure reference strains as calibrators, MS participants trended toward higher percentages of *C. perfringens* in fecal microbiota when compared to controls but this did not achieve statistical significance (Supplemental Figure 3, B-D). Of note, our estimates agree with the previously reported range (0.000001 - 0.01%) of *C. perfringens* abundance in fecal microbiota from healthy humans, confirming the organism's low-abundance (66, 74).

The 2018 revised classification scheme for *C. perfringens* defines 7 distinct toxinotypes based on carrying one or more of six major toxin genes (*plc/cpa, cpb, etx, iap* and *iab, cpe,* and *netB*) (27). We performed multiplex PCR for the major toxins used to characterize *C. perfringens* toxinotypes within our *etx*+ HC and MS populations (Figure 2F) (27). The majority of *etx*+ MS participants

harbor *C. perfringens* type D strains (*etx*+, *cpa*+) with fewer type B (*etx*+, *cpa*+, *cpb*+) strains detected (Figure 2F). *C. perfringens* enterotoxin (*cpe*), which is the main agent of *C. perfringens*-mediated human food poisoning, was not detected. Notably, unlike the more sensitive singleplex PCR (Figure 1C), *etx* and *cpa* appear to be absent in some participants by multiplex PCR, likely due to issues of annealing temperature compatibility among individual primer pairs in the multiplex PCR system. The apparent variations of *etx*/*cpa* band intensity ratios among participants, which differ from that of reference strains, suggest some participants likely harbor a community of combined type A strains (*cpa+*) and type B/D strains (*cpa+, cpb+, etx+* or *cpa+, etx+*).

We next examined the significance of *etx*-positivity in HC. Our multiplex PCR result suggests that there is a distinctive lack of or weakened *etx* band in the group of four etx-positive HC participants (Figure 2F) despite *etx* being clearly detected in singleplex PCR (Figure 1, B and C). To understand this phenomenon, we developed a sensitive TaqMan real-time PCR to simultaneously target *etx* and *cpa* genes and used the $2^{-\Delta\Delta Ct}$ analysis to quantify the relative abundance of *etx*-producing (*cpa*+, *etx*+) over non-*etx* strains (*cpa*+, *etx*-) from *etx*+ positive MS and HC groups (Figure 2G). The $2^{-\Delta\Delta Ct}$ value was computed to quantify fold changes of the *etx*/*cpa* ratio when a pure type D (*cpa*+, *etx*+) culture was used as a calibrator (72). A value of 1 was set as the $2^{-\Delta\Delta Ct}$ for the type D calibrator. We reasoned that $2^{-\Delta\Delta Ct} > 1$ indicates the dominance of *etx*-encoding strains with increased *etx*-plasmid copy numbers, and that $2^{-\Delta\Delta Ct} < 1$ indicates a higher percentage of *C. perfringens* type A (*cpa*+) in the bacterial community. Our results revealed significantly increased $2^{-\Delta\Delta Ct}$ values for the *etx/cpa* ratio in people with MS compared to HC (Figure 2H).

Since a $2^{-\Delta\Delta Ct}$ value ≥ 1 would suggest that 100% of a participant's *C. perfringens* strains are *etx*-harboring (i.e., type B and/or type D), we then obtained a maximum estimate of the average percentage of *etx*-harboring strains in the *C. perfringens* community for MS or HC. Our analysis shows that *etx*+ MS participants contain 32% *etx*-harboring strains and 68% non-*etx C. perfringens* strains (Figure 2I). In contrast, *etx*+ healthy controls contain 0.002% *etx*-harboring strains and nearly 100% non-*etx C. perfringens* strains. Analysis from a different perspective by quantifying the abundance of *etx* over *C. perfringens*-specific 16S rRNA yielded a higher estimate of the percentage of *etx*-harboring strains; 43% in MS and a lower percentage, 0.001%, in controls (Supplemental Figure 4).

Together, these data consistently show that people with MS are more likely to be colonized by *etx*+ strains of *C. perfringens* in their gut microbiome than are age and gender matched HC. Our data suggest that there is likely a yet to be defined threshold of relative abundance of ETX-producing strains, with relative abundance beyond this threshold contributing to MS. The complex dynamic between *C. perfringens* type A strains and the *etx*-encoding strains is likely important since type A strains compete with other *C. perfringens* strains for resources and because conjugative transfer between *etx* plasmid-harboring type D and *etx*-negative type A has been previously demonstrated *in vitro* (75).

Comparison of patient-derived, laboratory, and environmental isolates.

We next sought to determine if MS patient-derived isolates shared features with known environmental isolates and if they produced functional ETX. We conducted whole genome sequencing of an MS patient derived isolate (SHDS0050), several environmental isolates, including type D strains isolated from ruminants, and our laboratory type B strain. We successfully sequenced a closed 54.5 kb MS patient-derived plasmid, pSHDS0050 (Figure 3A). This plasmid contained 63 ORFs and an *etx* locus flanked by mobile genetic elements. As with other *etx* plasmids, pSHDS0050 had a Tn3 (in the opposite orientation) and an IS*1151* transposase upstream of *etx* (76), but had two IS*256* and a mutator type transposase directly after (Figure 3C). The plasmid resembled other highly conjugative plasmids of the pCW3 family that are found in *C. perfringens* strains, as it contained the *tcp* locus and other genes associated with conjugation (77) and the central control region containing the *parMRC* partitioning system (78). The plasmid lacked other toxin genes such as *cpe* or *cpb.* When comparing the MS patient derived type D plasmid to the other *etx*-containing type B and D plasmids sequenced in this study, pSHDS0050 maintained the same conserved genes such as *regB*, *pemK*, *amidoligase*, *permease*, RICIN domain containing genes, and a radical *SAM* gene (Figure 3C). Interestingly, pSHDS0050 had identical plasmid architecture to the sheep isolate NCTC8346 and the goat isolate FU17 (Figure 3C), which suggests ruminants may be a potential vector for infecting humans as originally hypothesized by Murrell (79). Although sharing much of the same genomic content, these type D plasmids were neither as large as the 64.7 kb *etx* plasmids sequenced in this study from type B strains ATCC3626 and NCTC3110 nor the published type B strain, NCTC8533 (Figure 3C)(80). pSHDS0050 lacked genes such as *cpb2*, *thiF* and *pri* present in those plasmids.

We next compared the circularized chromosomes of the type D strains CN3842, NCTC8346, and FU17, and the type B strains ATCC3626 and NCTC3110 to ensure that patient strain SHDS0050 was not a collection strain contamination. A GView BLAST atlas plot reveals that the patient-derived strain has multiple unique regions within its chromosome, distinguishing it from the other isolates (Figure 3B).

To evaluate production of epsilon protoxin (proETX) and pathogenicity, we cultured SHDS0050, the ATCC type B strain, and a ATCC type F strain in TGY broth, under anaerobic conditions, and then assessed supernatants for proETX by Western blot. The MS patient-derived strain produced an ~32.9 kDa proETX protein of similar mobility to the ATCC type B strain (Figure 3D). The ATCC type F strain was negative for ETX production, as anticipated. To evaluate cytotoxicity, harvested supernatants were treated with trypsin to activate ETX. Next, CHO cells expressing the human ETX receptor, MAL (hMAL-CHO) (54), or control CHO cells expressing GFP (GFP-CHO) were treated with trypsin-activated supernatants. Cell death was determined by propidium iodide (PI) exclusion assay. To confirm that the cytotoxic effects were ETX mediated, trypsin-activated supernatants were also treated with a neutralizing anti-ETX antibody (81) prior to CHO cell treatment. Only the trypsin-activated supernatants from the Lab type B and MS patient-derived type D strain, SHDS0050, induced hMAL-CHO cell death (Figure 3E). Cell death was not observed in hMAL-CHO cells treated with broth alone, and GFP-CHO cells were insensitive to all treatment conditions (Figure 3E). Anti-ETX antibody treatment inhibited hMAL-CHO cell death, indicating the supernatant cytotoxicity was ETX mediated. Collectively, these data indicate that our patient-

derived *C. perfringens* type D strain possesses typical type D plasmid architecture, is competent to produce functional ETX, and conceivably could have arisen from a ruminant source.

Single nucleotide polymorphisms (SNPs) in bacteria genes have been linked to microbial fitness (82) and the ability of pathogens to cause disease (83). Large-scale genomic analyses have identified abundant SNPs in the *C. perfringens* genome (84, 85). To characterize these variants, we collated 17 *etx* genes with coding DNA sequences (CDS) available through the National Center for Biotechnology Information (NCBI) database and performed a comparative alignment analysis. The SNP at site 762, carries the least conserved SNP among the 6 that we identified, and is the only SNP present in the coding sequence of activated ETX. At the 762 site, G substitutes for A as the minor allele regardless of *C. perfringens* toxinoptype (Supplemental Figure 5C).

The *etx* genes isolated from the human fecal samples in our study predominantly carry the minor allele at site 762 (95%, 20/21), 762G (Supplemental Figure 5D). This variant results in a synonymous mutation at residue 254 (Ser, corresponding to residue 222 in activated ETX) in the receptor binding domain (49). Emerging evidence indicates that synonymous mutations, previously assumed to be phenotypically neutral, contribute to microbial fitness. Furthermore, synonymous mutations can impact mRNA secondary structure, protein translation and protein folding (86).

ETX overcomes CNS immune privilege.

Circulating myelin-autoreactive lymphocytes are common in the general population (87). Despite the prevalence of myelin autoreactive lymphocytes amongst humans, widespread autoimmunity is minimized by mechanisms of peripheral tolerance and CNS barriers to preserve immune privilege (88-90). The importance of CNS barriers in maintaining immune privilege is well-demonstrated in active immunization models of EAE. In this model system, animals are immunized with a myelin antigen, typically a myelin specific protein or peptide, in complete Freund's adjuvant (CFA) (91). In most paradigms, immunized animals do not develop clinical or histologic CNS disease unless they also receive PTX, which targets CNS endothelial cells at the BBB (91-93). Similarly, in many myelin peptide-specific T cell receptor (TCR) transgenic models, EAE occurs infrequently unless animals receive PTX, despite the TCR repertoire being biased toward unusually high frequencies of autoreactive clones (91, 94). Although PTX is extensively used in EAE to overcome immune privilege, it is clinically irrelevant to MS.

Knowing that blood-borne ETX specifically targets CNS endothelial cells (26), we wanted to test if ETX was sufficient to breach CNS immune privilege in the presence of circulating myelin autoreactive lymphocytes, and adapted a widely-used immunization model of EAE using the immunodominant peptide in the myelin oligodendrocyte glycoprotein (MOG) (91). On day 0, female C57BL/6 mice received a subcutaneous (SC) injection of 200 µg of synthesized mouse MOG_{35-55}, emulsified in 50 µl of CFA. On days 0 and 2, mice received either PTX at 5 µg/kg body weight (~100 ng per mouse), ETX at 50 ng/kg body weight (~1 ng per mouse), or ETX at 500 ng/kg body weight (~10 ng per mouse), all delivered intraperitoneally (IP).

ETX, like PTX, was sufficient to induce clinical disease in mice immunized with MOG_{35-55} (Figure 4A). In the absence of either toxin, MOG_{35-55} immunized animals remained healthy, without an observable phenotype. Disease activity induced by ETX occurred at doses significantly lower than that of PTX (5 ng/kg or 50 ng/kg for ETX, and 5μg/kg for PTX). Onset, temporal course, and peak clinical deficits were similar for ETX- and PTX-induced EAE when using the classical EAE scoring scale (Figure 4A). The magnitude of demyelination in the spinal cord and the ultrastructural characteristics of demyelination were similar comparing ETX-induced EAE (ETX-EAE) to PTX induced EAE (PTX-EAE, Figure 4, B and C). These results indicate that ETX is a potent inducer of EAE in the context of a MOG_{35-55}/CFA immunization paradigm.

ETX-EAE induces multi-focal demyelination.

ETX-EAE groups displayed a wider array of behavioral deficits when compared to PTX-EAE, including ataxia, head tilt, imbalance, axial rotation, and left/right leaning, as captured by the atypical EAE scoring scale (Figure 5A and Supplemental Figure 6). Demyelination in PTX-EAE mice was largely restricted to the spinal cord (Figures 4 and 5). In contrast, ETX-EAE mice developed multifocal demyelination more typical of MS (Figure 5B). Compared to PTX-EAE, ETX-EAE mice had nearly twice as many lesions in the cerebellum, and lesions in the corpus callosum were only observed in the ETX-EAE group (Figure 5C). ETX-induced EAE showed perivenular cuffs of mononuclear cells and mononuclear infiltrates that correlated with demyelination (Supplemental Figure 7).

We next wanted to compare the immune infiltrates in brain and spinal cord between the ETX- and PTX-EAE models. We examined histologic sections in ETX-EAE, PTX-EAE, and controls for infiltrating CD4+ lymphocytes. While both models induce similar demyelination in the spinal cord, PTX-EAE shows significantly more infiltrating CD4+ T cells in the spinal cord compared to ETX (Figure 6, A and E). For the cerebellum, there are significantly more infiltrating CD4+ lymphocytes and more CD4+ lymphocytes in perivascular cuffs in the ETX-EAE model compared to PTX-EAE (Figure 6, B-F). In the thalamus, there was a similar trend toward more peri-venular CD4+ T cell infiltrates in ETX-EAE when compared to PTX-EAE (Figure 6, C-F). In the spinal cord, similar activation of inflammatory processes was observed in both models at peak disease, based on immunohistochemical analysis of phospo-NFκB p65, CD68, and CD45 (Figure 7 and Supplemental Figure 8). In the cerebellum, however, CD68 is significantly increased in ETX-EAE but not PTX-EAE mice (Figure 7, A-C). A similar trend was also observed in the cerebellum for phospo-NFκB p65 and CD45, but this did not achieve statistical significance (Figure 7 and Supplemental Figure 8). These results, collectively with data from figures 4 and 5, indicate that ETX induces multifocal, inflammatory demyelination in a neuroanatomic distribution more consistent with MS, and with a stronger correlation between immune infiltrates and demyelination in the ETX-EAE model compared to PTX-EAE (Supplemental Figure 9).

Human lymphocytes, but not mouse lymphocytes, express the ETX receptor, MAL (54, 58, 95). While it seemed unlikely that ETX functions to induce active EAE by affecting peripheral immunity, we nevertheless wanted to test this possibility through tracking MOGp-specific T cell cytokine responses via antigen recall experiments. To track the fate of MOGp-specific T cell

responses *in vivo* (96-98), we transferred naïve, purified $MOGp_{35-55}$-specific $CD4^+$ T cells from 2D2 transgenic mice into recipient wild-type B6 mice 24 hours prior to induction of active EAE by subcutaneous immunization with $MOGp_{35-55}$ in CFA. Immunized mice then received either PBS, 10 ug/kg PTX, or 500 ng/kg ETX immediately after immunization and 48 hours later (Supplemental Figure 10A). We monitored mice for onset of clinical disease (Supplemental Figure 10B) and fourteen days following immunization, we generated single cell suspensions from inguinal lymph nodes, cervical lymph nodes and from the CNS (brain and spinal cord) and processed these for either 1) direct analysis of basal cytokine production by flow cytometry (Supplemental Figure 10C) or 2) for *ex vivo* re-stimulation with $MOGp_{35-55}$ for 72 hours to determine cytokine production after antigen recall (Supplemental Figure 10D). For both sets of experiments we assessed intracellular cytokine production by flow cytometry. MOGp-specific 2D2 were positively defined as $CD45^+$, $CD3/5^+$, $CD4^+$, and $Thy1.1^+$. Frequencies of TNFα, IFNγ, or GM-CSF positive $CD4^+$ T cells did not significantly differ between PBS controls and ETX-treatment in cervical or inguinal lymph nodes, except for a small difference in the frequency of TNFα positive T cells from inguinal lymph nodes, following 72 hours of re-stimulation with MOG_{35-55} (Supplemental Figure 10D). In CNS tissue, there were no differences noted in the frequencies of TNFα, IFNγ, or GM-CSF positive $CD4^+$ T cells between the ETX and PTX treatment groups. These results support the conclusion that ETX is not functioning through significant effects on peripheral immunity and does not impact MOGp-specific T cell responses during the induction of active EAE.

ETX and PTX alter the CNS endothelial cell transcriptome to induce genes involved in BBB dysfunction.

To gain insight into mechanisms for how ETX and PTX might function in overcoming immune privilege at the CNS endothelial barrier, we conducted bulk RNA-seq on CNS endothelial cells isolated from animals treated with ETX, PTX, or PBS and compared transcriptional profiles.

Mice were treated with PBS, ETX (0.5 µg/kg b.w.), or PTX (5 µg/kg b.w) on two consecutive days followed by isolation of CNS endothelial cells from spinal cord for bulk RNA-seq. CNS endothelial cells were isolated from spinal cords, as previously described (99) 16 hours after the second toxin dose. Bulk RNA-seq was performed and analyzed using the limma-voom workflow (100). Principal-component analysis (Figure 8A) revealed separation by treatment. PC1 distinguished control from both ETX and PTX, whereas PC2 distinguished ETX from PTX, indicating that the ETX and PTX transcriptomes are more like each other than PBS controls. We identified 798 differentially expressed genes (DEGs) between ETX and PBS treated samples, and 905 DEGs between PTX and PBS treated samples (FDR q-values < 0.10). Of these DEGs, 595 changed in response to both ETX and PTX treatments (Figure 8B). Comparing the fold changes (FC) of the overlapping genes revealed a remarkable consistency in direction and magnitude of differential expression between ETX and PTX treatments (Figure 8C). Considering that PTX is an A-B toxin that functions through ADP-ribosylation of G-proteins and that ETX is a pore forming toxin of the aerolysin family, the consistency in induced and suppressed genes was both intriguing and unexpected. A heat map displaying genes of interest revealed induction of protease, signal transduction, cytokine, and transcription factor genes potentially relevant to overcoming CNS

immune privilege (Figure 8D). In figure 8E, we show a heat map of genes differentially expressed by ETX and PTX that also were identified by Munji et al. as components of a core set of genes involved in BBB dysfunction (101). The overall gene induction in endothelial cells isolated form PTX or ETX-treated mice shares a great degree of overlap (Figure 8F). Further analysis with of the RNA-seq data identified signaling pathways preferentially activated by ETX (Figure 8G).

Discussion

We presume the factors responsible for the formation of the initial lesions in MS are the same factors responsible for new lesion formation throughout the course of the disease. That is, environmental triggers for MS likely do not occur once at disease initiation, but rather, arise repeatedly throughout the course of disease. The episodic nature of MS disease activity aligns well with the ETX hypothesis. ETX production occurs when *C. perfringens* types B or D enter log-phase growth and is thus tied to increased abundance of these strains in the gut microbiome (28, 50). Brief cycles of log-phase growth, followed by long periods of quiescence, would account for episodic ETX production. MS disease activity is linked to an increased relative abundance of Bacillota (Firmicutes), which includes the Genus *Clostridium*, suggesting that the MS gut microbiome episodically favors growth of this Phylum (11). In addition to our findings, it is notable that the species, *C. perfringens*, is the most highly associated bacteria with neuromyelitis optica; an immune-mediated, demyelinating disorder affecting the spinal cord and optic nerve (102, 103).

C. perfringens type D is responsible for enterotoxemia in sheep, goats, and less frequently, in cattle (104). The disease has worldwide distribution and can be acute, sub-acute, chronic, or fatal (105, 106). Although enterotoxemia type D is an infectious disease that can occur in the form of small outbreaks via the oral-fecal route, it is not a typical contagious disease. A variable number of ruminants harbor *C. perfringens* type D in their small intestine, but microorganism numbers are generally small and clinical disease does not occur unless the intestinal microbial balance is disrupted (106, 107). When large quantities of readily fermentable carbohydrates are fed to these animals, undigested starch passes into the small intestine and provides a substrate for *C. perfringens* to proliferate rapidly. This is followed by production of large amounts of ETX, which is then absorbed into the systemic circulation. The bacteria are passed by feces into the environment and can survive for several months in the soil. Neonates and older animals become infected via the fecal-oral route.

The Epstein Barr Virus (EBV) has been proposed as an environmental trigger for MS (108), potentially functioning through molecular mimicry (109). In humans, EBV is significantly associated with MS, but seroconversion is itself not sufficient to induce MS as ~94% of the general population is seropositive by age 24, yet MS risk remains relatively low (108, 110, 111). This suggests that while EBV may play an role in MS pathogenesis, an additional, but less widely distributed causal factor, as discussed by Carl Nathan (112), is required, which we propose to be *C. perfringens* type B or D.

In summary, we find a strong clinical association between a specific bacterium, its toxin, and a diagnosis of MS. In addition, we find that the abundance of ETX-producing strains of *C. perfringens* is significantly elevated in the MS gut microbiome. We provide a biologically plausible mechanism by which ETX functions in the multistep process of CNS autoimmunity. Ultimate proof of this hypothesis, as would be the case for any environmental factor, will require a clinical trial to neutralize ETX or to eliminate *C. perfringens* type B or D in the human host.

Methods

Details on participant recruitment, reagents, and experimental methods are found in supplemental materials.

Statistical Analysis

Statistical analysis was performed using GraphPad Prism (v.9; GraphPad) and Microsoft Excel (2016; Microsoft). Data of Gaussian distribution are represented as mean ± SEM (standard error of the mean) or SD (standard deviation) as indicated. Data of non-Gaussian distribution are represented as median ± range. Unpaired two-tailed t-test (for Gaussian distribution) or Mann–Whitney test (non-Gaussian distribution) were used to compare two datasets for statistical significance. For multiple datasets, one-way ANOVA followed by post hoc Tukey's multiple comparisons test (for Gaussian distribution), Kruskal–Wallis test followed by post hoc Dunn's multiple comparisons test (for non-Gaussian distribution), or two-way ANOVA with Sidak's multiple comparisons test were carried out to determine statistical significance as indicated. For EAE time course analysis, non-parametric Friedman test followed by post hoc Dunn's test was performed. Pearson's correlation analysis was performed to examine whether the density of CNS infiltrating lymphocytes correlates with the extent of demyelination. One phase decay model was employed for curve fitting. Multivariable logistic regression was used to test the difference while adjusting for covariates. p values are stated in figures and legends.

Data and materials availability

C. perfringens chromosome and plasmid sequences were deposited into GenBank under the following accession numbers (chromosome, plasmid for each strain): *C. perfringens* type D CN3842 (CP116428, CP116429), *C. perfringens* type D NCTC8346 (CP116430, CP116431), *C. perfringens* type D FU17 (CP116432, CP116433), *C. perfringens* type D SHDS0050 (CP116434, CP116435), *C. perfringens* type B NCTC3110 (CP116436, CP116437), and *C. perfringens* type B ATCC3626 (CP116438, CP116439).

The RNA-seq data discussed in this publication have been deposited in NCBI's Gene Expression Omnibus (Edgar et al., 2002) and are accessible through GEO Series accession number GSE223137

https://www.ncbi.nlm.nih.gov/geo/query/acc.cgi?acc=GSE223137

Study Approval

The Harboring the Initial Trigger(s) for Multiple Sclerosis (HITMS) Study, protocol # 1003010940, was approved by the Weill Cornell Medicine Institutional Review Board. All study participants received, reviewed, and signed a written informed consent.

The Weill Cornell Medicine Institutional Animal Care and Use Committee (IACUC) approved all experimental procedures with animals, which were also consistent with the ethical guidelines of the National Institutes of Health.

Author Contributions

Y.M. Conceptualized, designed, and carried out EAE experiments and performed histological and ultrastructural analyses. He conceptualized quantification methods and carried out the analyses of fecal samples by standard and TaqMan real-time PCR. Wrote the IACUC protocol. Edited manuscript.

D.S Conceptualized, designed, and carried out the purification of bacteria from fecal samples using the Nycodenz method, performed the genomic assembly of the human *C. perfringens* isolates, and created the plasmid maps for the patient and environmental isolates. Edited manuscript.

J.R.L. Generated the antibodies used in the detection of ETX. Assisted with the design of the study and analysis of *etx* detection in fecal samples from MS and HC study participants. Assisted with obtaining the MS participant isolate. Conducted the analysis of CHO cell cytotoxicity. Isolated endothelial cells and purified RNA from mice used in the analysis of differential gene expression. Assisted with writing the IRB and IACUC protocols. Edited manuscript.

S.H. Assisted in the analysis of fecal samples and purification of isolates.

B.Z. Performed standard and TaqMan real-time PCR analyses of fecal samples. Assisted with daily monitoring and scoring of EAE mice in all experiments involving the model.

J.B.G Designed, conducted, and analyzed the EAE antigen recall and flow cytometry experiments.

P.Z. Conducted the analysis of endothelial cell differential gene expression. Constructed the principal component analysis plot, gene ontogeny plot, and heat maps for endothelial cell differential gene expression.

F.D. Assisted in the design, analysis, and strategy for endothelial cell differential gene expression.

D.J.B. Performed Ilumina shotgun sequencing and Nanopore long reads on purified bacterial isolates. Edited the manuscript.

C.P.P. Advised and assisted with CNS endothelial cell isolation and preparation of RNA for bulk RNA seq experiments.

K.T. Edited the manuscript.

P.W. Performed Western blot analysis on supernatants from clinical isolates.

K.R.R. Assisted with design of the study, interpretation of data, and edited the manuscript.

S.G. Assisted with design of the study. Developed the RedCap database for entering secure demographic and clinical information on recruited subjects. Edited the manuscript.

V.A.F. Assisted with the design of the study, interpretation of results, and edited the manuscript.

B.M. Assisted with the analysis and interpretation of the plasmid maps for patient derived strains and environmental strains. Edited the manuscript.

F.U. Provided the *C. perfringens* types B and D environmental isolates. Provided background on *C. perfringens* type D in ruminants. Edited the manuscript.

L.Z. Recruited patients for the study. Maintained the database.

M.M. Assisted with Western blot experiments and figure preparation.

R.R. Edited the manuscript.

E.B. Edited the manuscript. Assisted with antigen recall experiments.

D.D. Assisted with plasmid assemblies.

J.P. Recruited patients for the study.

U.K. Recruited patients for the study.

N.N. Recruited patients for the study.

I.B. Edited the manuscript.

Z.C. Reviewed the power calculation for the analysis of *etx* in human fecal samples, multivariable logistic regression, and reviewed all statistical methods.

D.B. Supervised and designed the bioinformatics approach for endothelial cell differential gene expression.

R.D. Assisted with design of the transcriptional profiling experiments and interpretation of the RNA seq datasets. Designed the strategy for isolation of CNS endothelial cells from whole animals for bulk RNA seq.

G.S. Conceptualized, supervised, and interpreted the EAE experiments.

C.M. Designed the sequencing strategy for *C. perfringens* strains.

T.V. Conceptualized and supervised the overall study. Conceptualized and designed the analysis of fecal samples for *etx* detection. Conceptualized the EAE experiments. Conceptualized and designed the CNS endothelial cell RNA seq experiments. Analyzed and interpreted data from the *etx* detection, and EAE, CNS endothelial cell RNA seq experiments. Was responsible for writing and adhering to the IRB and IACUC protocols. Wrote the manuscript.

The order of the co–first authors was based on the time and effort devoted to this project.

Acknowledgments

We received technical assistance from Fengxia Liang, Chris Petzold, and Kristen Dancel-Manning at the Electron Microscopy Core of New York University for ultrastructural analysis. We thank the Weill Cornell Genomics Core for sequencing the Illumina samples on their NovaSeq S4 and assisting with demultiplexing. We thank Regina Alice Schroeder, Samantha Shetty, Mason Kruse-Hoyer, Melanie Marcille, and Nicole Zinger for their help in recruiting study participants. Most importantly, we are grateful to all the people with MS who volunteered to participate in the HITMS study. Illustrations were made in BioRender. This work was supported by National Multiple Sclerosis Society Research Grant RG4965A4 (T.V.), National Institutes of Health grant R21 RNS106581A (T.V.), National Institutes of Health grant R01AI162936 (G.F.S.), National Multiple Sclerosis Society Career Transition Award TA-1604-08444 (J.R.L.), National Institutes of Health Medical Scientist Training Program grant (T32GM007739) to the Weill Cornell/Rockefeller/Sloan Kettering Tri-Institutional MD-PhD Program (E.B.), National Institutes of Health grants R01AI151059 and R01MH117406 (C.E.M.), and generous gifts from the Diane Kemper Goldman Trust, and the Wilma S and Laurence A Tisch Foundation.

Conflict of interest

Y.M., J.R.L., K.R.R, V.A.F. and T.V. are inventors on a patent application for a method to diagnose and treat multiple sclerosis using anti-ETX monoclonal antibodies. R.R., Y.M., J.R. L., K.R.R, V.A.F. and T.V. own equity in Astoria Biologica.

Figures and figure legends

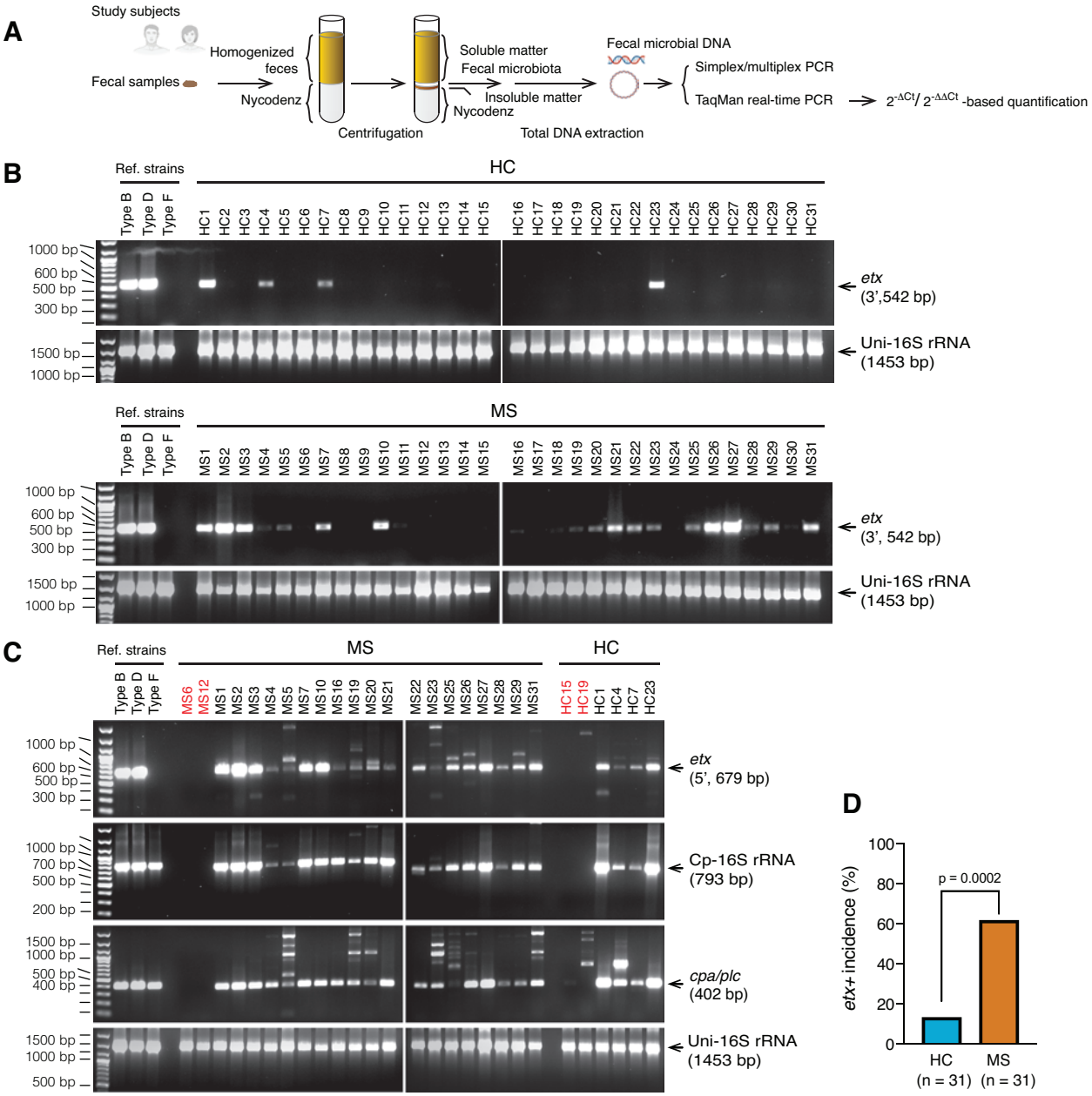

Figure 1. Prevalence of *etx* in the gut microbiome of people with MS and Healthy Controls (HC). (**A**) Workflow of the experimental setup. Fecal bacteria were purified by density gradient centrifugation in a Nycodenz solution. (**B**) Initial screen by PCR targeting the 3'-terminal sequence of *etx* (542 bp) detected more frequent presence of *etx* in people with MS compared to HC. (**C**)

Confirmatory assays for *etx*+ participants from the initial screen (B) using PCR for *C. perfringens*-specific genes. PCRs targeting the 5'-terminal sequence of *etx* (679 bp) confirmed the initial detection results. Detection *of C. perfringens*-specific 16S rRNA and the chromosomally located alpha toxin (*cpa/plc*) gene present in all *C. perfringens* strains corroborates the source of the *etx* gene. Participants labeled in red are included as known *etx*-negative samples from (B) and included for comparison. Reference strains including *C. perfringens* type B (ATCC3626), type D (FD203), and type F (ATCC12915) were included as additional controls. Type B and D are *etx*-harboring strains and type F is negative for *etx*. Type B, D, and F are all positive for *cpa/plc* and *C. perfringens*-specific 16S rRNA. (**D**) Statistical analysis of *etx* frequency by Fisher's exact test. Similar results were achieved in three independently repeated PCR experiments using the same subjects.

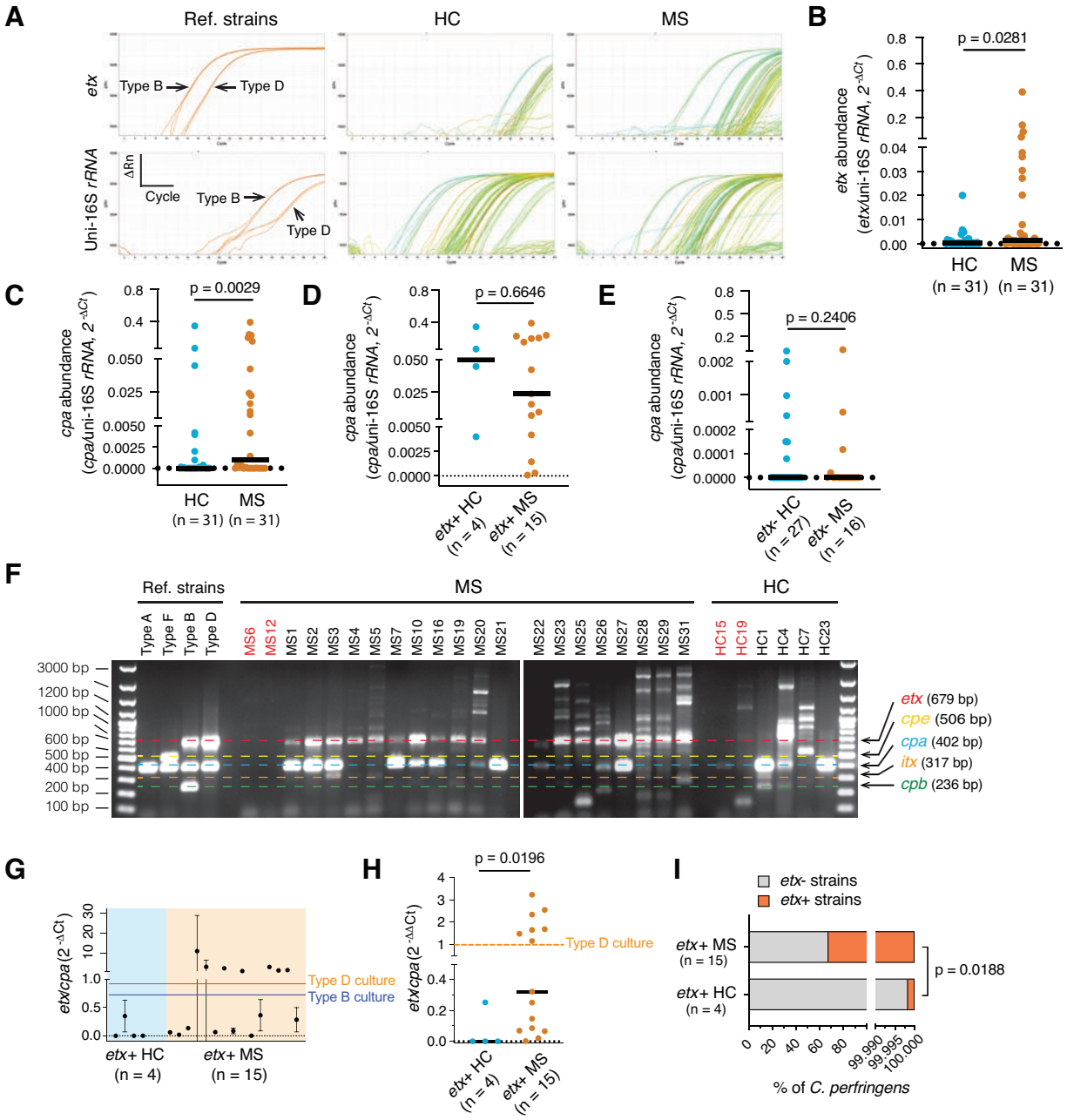

Figure 2 *etx* abundance and *etx*-harboring strains increase in the fecal microbiota of MS.

(**A**-**B**) Representative amplification plots (A) and statistical analysis of *etx* abundance (B) by TaqMan real-time PCR analysis. Of note, the system detected 15 *etx*-positive MS, fewer than what was detected by standard PCR (19). (**C**-**E**) *cpa* abundance in healthy control (HC) and MS.

(**F**) Multiplex PCR reveals different composition of strains in the fecal *C. perfringens* community from *etx*-positive participants. Participants labeled in red are included as known *etx*-negative samples from (1B) and included for comparison. Of note, *C. perfringens* type E, defined by the presence of *cpa* and *itx*, is present in MS3, MS31, and HC1; while MS19, MS26, HC1, and HC4 carry *cpb*, a virulence determinant carried by *C. perfringens* type C and *C. perfringens* type B. (**G**-**I**) Analysis of *etx*/*cpa* ratio by TaqMan real-time PCR using the *C. perfringens* type B (ATCC3626) and type D (FD203) strains as a calibrator for the quantification of *etx*+/*etx*- strain ratios in the fecal microbiota from *etx*+ participants. Quantification of the ratio of *etx*/*cpa* by $2^{-\Delta Ct}$ (G), *etx*/*cpa* against type D culture as calibrator by $2^{-\Delta\Delta Ct}$ (H). Dashed horizontal lines in G and H show $2^{-\Delta Ct}/2^{-\Delta\Delta Ct}$ values from culture of indicated reference strains. Estimate of maximum of percentages of *etx*- and *etx*+ strains in *etx*+ HC and MS fecal microbiome (I). The estimates assume that the subjects with a $2^{-\Delta\Delta Ct}$ value above 1 (type D) contains 100% *etx*+ strains. p-value determined by Mann-Whitney test (non-Gaussian distribution). Number of subjects (n) is indicated in individual panels; black lines in B, C-E, and H indicate medians. Data in G are mean ± SD, n = 3 technical triplicates in a representative real-time PCR experiment). Similar results were achieved in three independently repeated PCR/qPCR experiments using the same subjects.

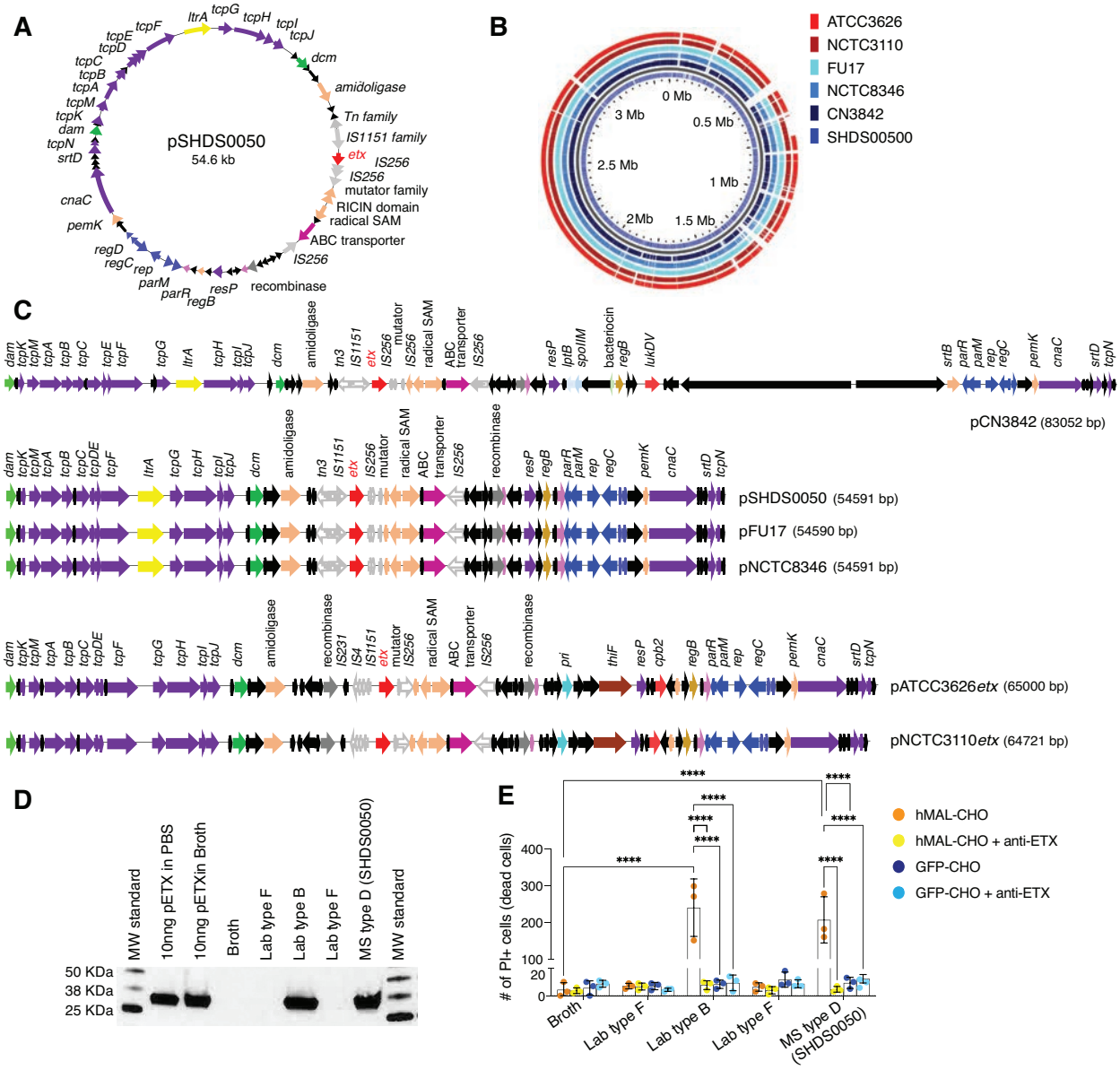

Figure 3. Characterization of patient derived strain SHDS0050 and its comparison to environmental and laboratory ETX-producing strains. (**A**) The circular map of *etx*+ plasmid (pSHDS0050) from a MS patient-derived SHDS0050 strain. Hypothetical and proteins of unknown function ORFs are colored black, those involved in conjugation are purple, toxin ORFs are red, DNA methylases are green, transposases and recombinases are gray, ribonucleases are pink, plasmid replication ORFs are blue, conserved *etx* plasmid ORFs are red, and ABC transporters are

magenta. (**B**) GView BLAST Atlas map comparing the circular chromosomes of pSHDS0050 as the reference genome to *etx*+ strains CN3842, FU17, and NCTC8346, ATCC3626, and NCTC3110. Type D chromosomes are shades of blue, while type B are shades of red. Colored regions for genomes indicate a BLAST hit present in the reference genome. Empty slots indicate no matching hits. SHDS0050 genome is distinct from other strains. (**C**) Linearized plasmid map comparisons comparing pSHDS0050 with the *etx* plasmids of three type D collection strains pCN3842, pFU17*etx*, and pNCTC8346*etx*, and two type B strains pATCC3626*etx* and pNCTC3110*etx*. The linearized maps use the same color scheme as A, with different transposase ORFs having different pattern fillings. The three type D strains share the same gene content and share many of the same genes. (**D**) Western blot analysis for pETX production from indicated *C. perfringens* strains. pETX spiked into PBS or broth were used as positive controls. Broth only was used as a negative control. (**E**) Susceptibility of hMAL-CHO or GFP-CHO cells to activated ETX. To confirm if cell death was ETX mediated, broth was pretreated with a neutralizing anti-ETX antibody. Broth alone was used as a negative control. Cell death determined by PI staining. $n = 3$. $p < 0.0001$ determined by two-way ANOVA with Sidak's multiple comparisons test.

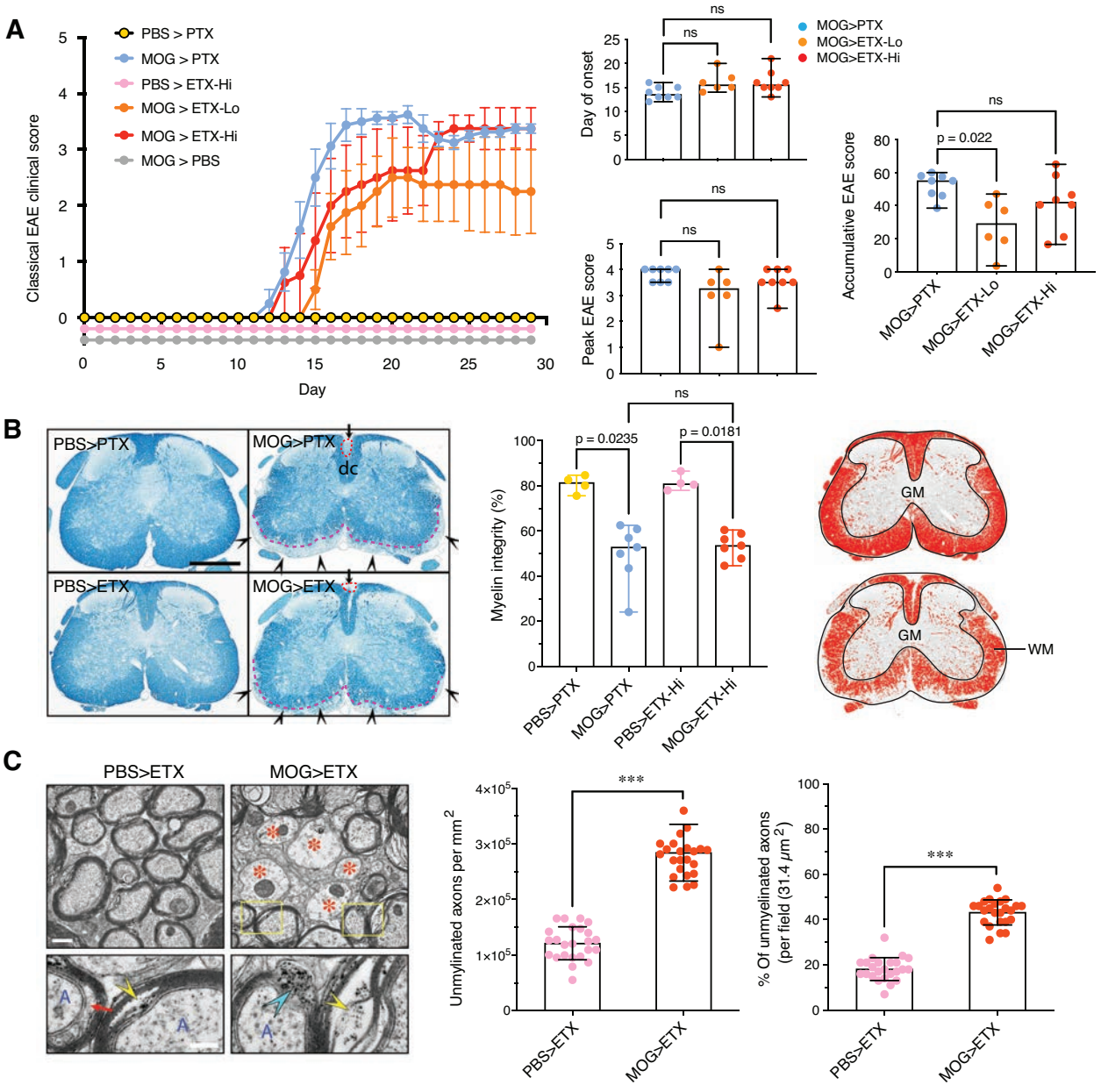

Figure 4. Comparison of ETX- and PTX-EAE in the spinal cord using the classical scoring scale. (**A**) Classical EAE time-course (left panel) of mice from indicated experimental groups. Mice immunized with CFA/PBS (PBS) or CFA/MOG_{35-55} (MOG) were injected intraperitoneally with PTX at 5 µg/kg, ETX at 50 ng/kg (ETX-Lo), or ETX at 500 ng/kg body weight (ETX-Hi) on day 0 and 2 following immunization. Quantification of day of disease onset, peak EAE score, and accumulative

EAE score (right panels). (**B**) Representative sections of lumbar spinal cord from mice sacrificed at day 30 stained with Luxol Fast Blue (myelin stains blue). Red circles and black arrowheads indicate demyelination in the dorsal column (dc) or in the lateral and ventral funiculi, respectively. Dashed pink lines indicates lesion border in ventral white matter (WM) tracts. Quantification of myelin integrity (%, middle panel) generated from binary images (right panel). (**C**) Electron microscopy (left panel) and quantification (middle and right panels) evaluating demyelination in ETX-EAE mice. Red asterisks indicate demyelinated axons; yellow rectangles highlight ultrastructural changes of myelin sheath; cyan arrowhead indicate de-compacted myelin sheath; yellows arrowheads indicate splitting myelin sheath and debris; red arrow indicate expanded space between an axon and myelin. Data in left panel of A are means ± SEM; data in right panels of A and B represent median $\pm$ range; Kruscal-Wallis test (non-parametric); ns, not significant; n = 4 mice for PBS>PTX and PBS>ETX-Hi controls, n = 6 mice for MOG>EAE-Lo, and n = 8 mice groups MOG>PTX and MOG>ETX-Hi. Data in C represent mean $\pm$ SD; unpaired t-test; *** $p < 0.001$; n = 24 fields from 2 mice. Scale bars, 1 mm in B, 500 nm (top panels) and 200 nm (lower panels) in C. Similar results for two independent experiments.

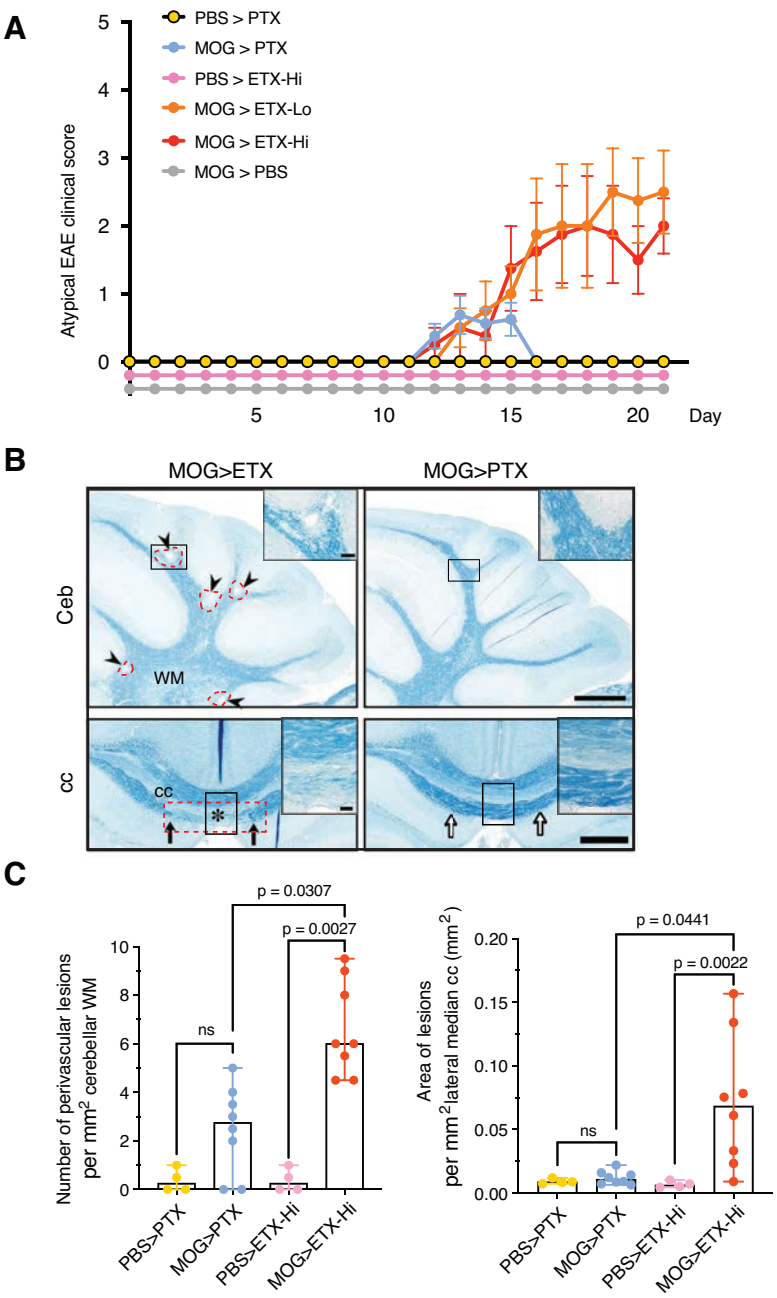

Figure 5. ETX-EAE is characterized by multifocal demyelination in the CNS. (**A**) ETX-EAE mice developed atypical EAE, which is characterized by ataxia, along with classical EAE symptoms defined by ascending paralysis. Same treatment conditions as in figure 4, CFA/MOG_{35-55} followed by ETX (ETX-EAE) or PTX (PTX-EAE). (**B**) ETX targets broader brain regions compared to PTX including cerebellum (Ceb) and corpus callosum (cc). ETX-EAE mice (left column) exhibit more

focal demyelinating lesions (arrowheads and red dashed circles) in the cerebellum and corpus callosum within WM tracts when compared to PTX-EAE mice (right column). Asterisk in lower row indicates demyelinated cc. Black arrows indicate borders of a cc lesion, which is also framed with a red dashed rectangle. A corresponding location in PTX- EAE mice (right column) is indicated by white arrows. Regions framed with black boxes are shown at high magnification in inserts. (**C**) Quantification of lesions in the cerebellum and corpus collosum. Data in A are means ± SEM, and data in C represent median ± range; Kruscal-Wallis test (non-parametric). n = 4 mice for PBS>PTX and PBS>ETX-Hi controls, n = 6 mice for MOG>ETX-Lo, and n = 8 mice for groups including MOG>PTX and MOG>ETX-Hi. ns, not significant. Scale bars, 1 mm in B and 100 µm in the inserts. Similar results were achieved in two independently repeated experiments.

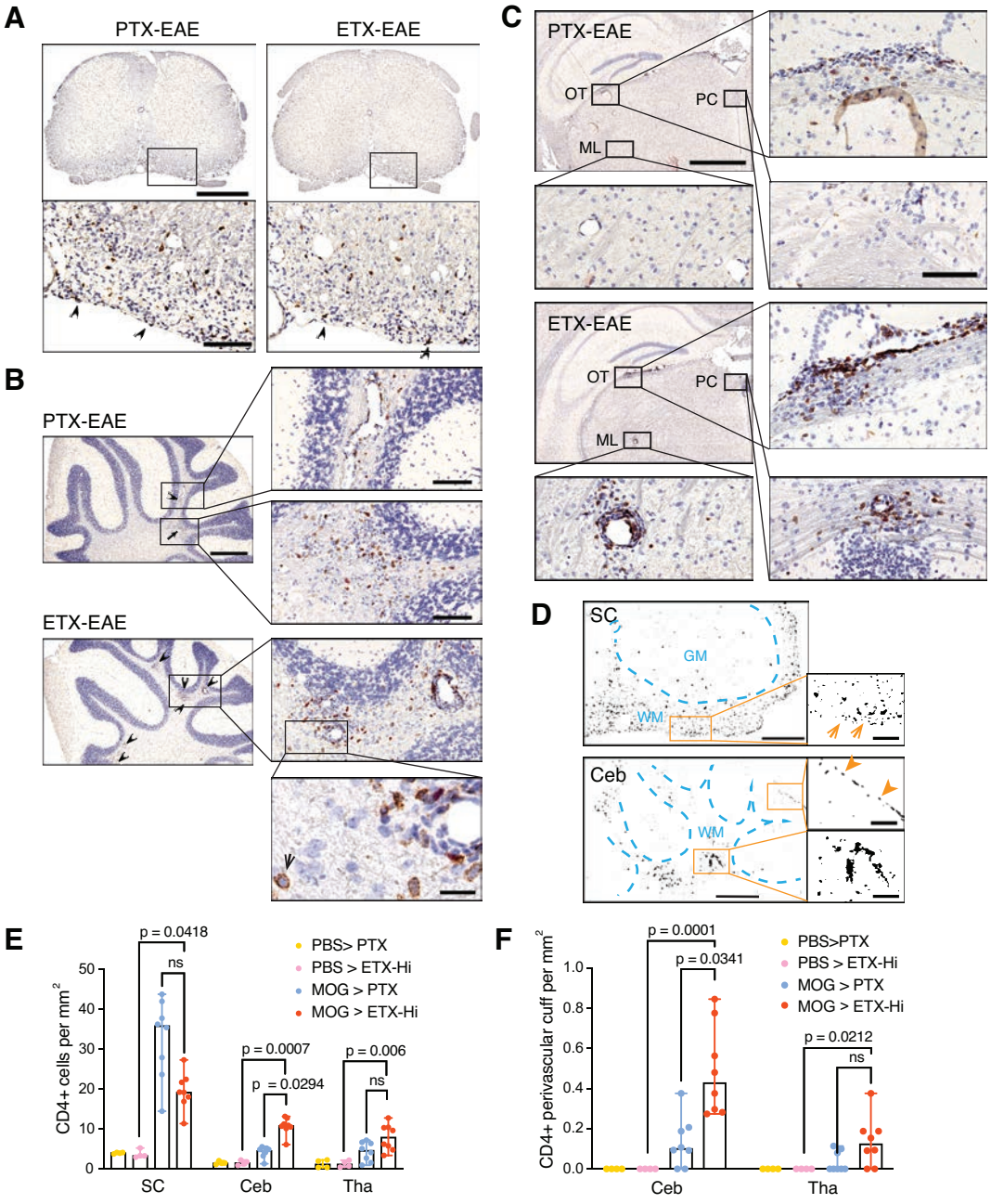

Figure 6. ETX-EAE mice show increased CD4+ lymphocyte infiltration in the cerebellum and thalamus compared to PTX-EAE. Sections from mice sacrificed at day 30 post-immunization with CFA/MOG_{35-55} followed by ETX (ETX-EAE) or PTX (PTX-EAE) injection were immunostained with anti-CD4 antibody (brown) and counter-stained with hematoxylin (purple). (**A**-**C**) Representative

CD4 staining in spinal cord (A), cerebellum (B) and thalamus (C). In ETX-EAE mice, CD4+ cells were found in perivascular cuffs and surrounding parenchyma indicated by arrowheads and shown in boxed regions of B and C. CD4+ cells from PTX-EAE mice were localized to perivascular space or scattered (arrowhead and arrow). Boxed regions shown at higher magnifications to illustrate morphological details. A high magnification micrograph (bottom panel in B) depicts positive CD4 staining (black arrow). OT, optic tracts; ML, medial lemniscus; PC, posterior commissure. (**D**) ImageJ-generated binary drawings on CD4+ distribution in the white matter (WM) of a PTX-EAE spinal cord (SC, orange arrows) and ETX-EAE cerebellum (Ceb). In Ceb, orange arrowheads indicate CD4+ cells confined to a single layer in the SC meninges of PTX-EAE mouse (upper boxed region). Perivascular localization of CD4+ cells shown at a higher magnification in cerebellum of ETX-EAE mouse (lower boxed region). GM, gray matter. Scale bars, 1 mm (top row A, and left column B), 2 mm (top and third rows in left column in C), 200 µm (high magnification of boxed regions A-C), 500 µm (D, left column), 100 µm (D, right column), 50 µm (B, bottom right panel). (**E** and **F**) Quantification of number of CD4+ cells (E) and CD4+ perivascular cuffs (F) in indicated CNS regions. Data represent median $\pm$ range; Kruscal-Wallis test (non-parametric). ns, not significant. n = 4 and 8 mice for controls (PBS>PTX; PBS>ETX-Hi) and EAE groups (MOG>PTX; MOG>ETX-Hi), respectively. Similar results were obtained from two independent experiments.

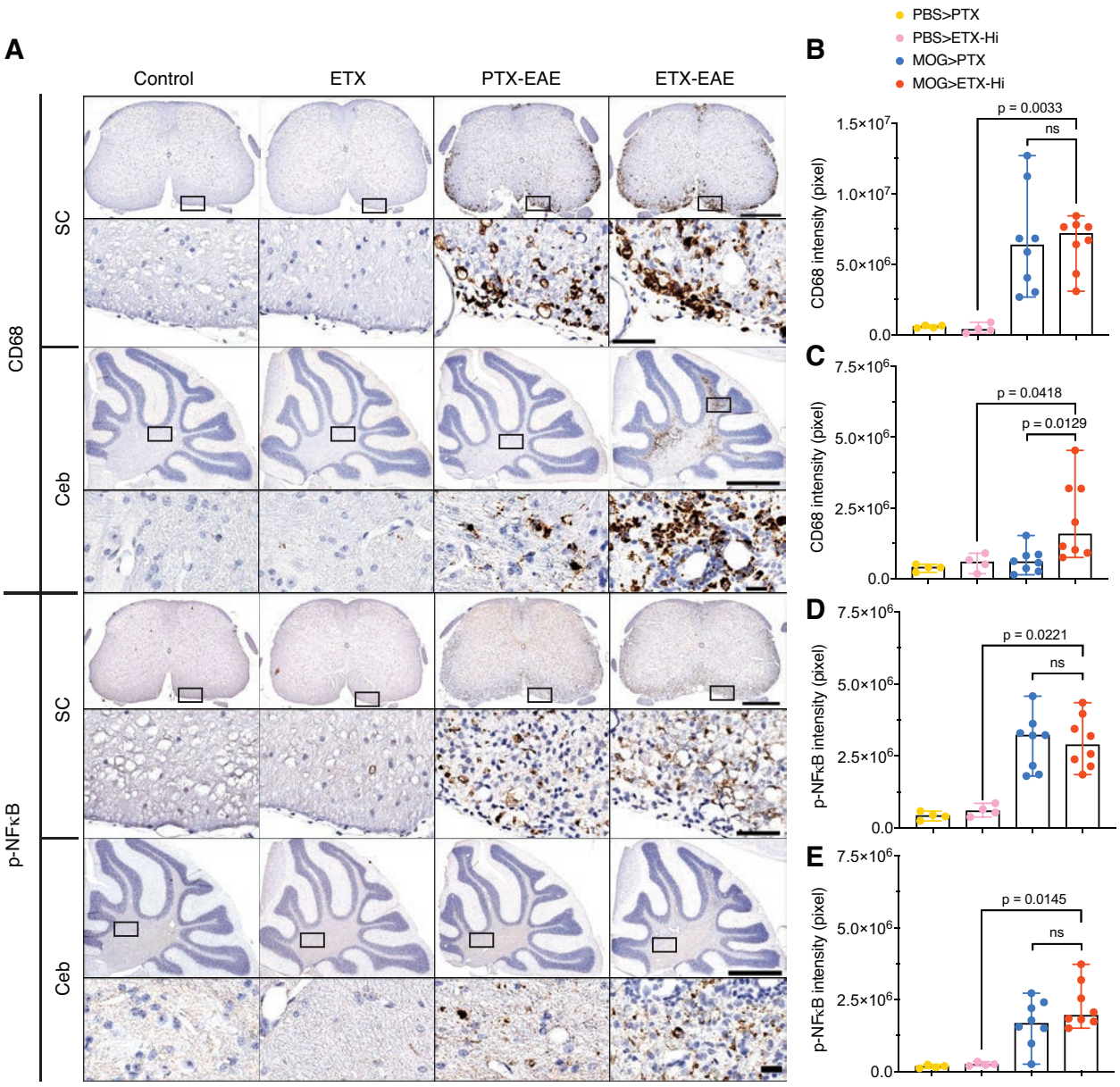

Figure 7. ETX-EAE mice show increased CD68+ microglia in the cerebellum of ETX-EAE mice compared to PTX-EAE mice, despite similar activation in the spinal cord and a comparable profile of transcription factor NFκB p65 in both models. (**A**) Representative sections from mice sacrificed at day 30 post-immunization with CFA/MOG_{35-55} and followed by either ETX (ETX-EAE) or PTX (PTX-EAE) injections were immunostained with anti-CD68 antibody or anti-phospho-NFκB

p65 (Ser 276). A rectangle-framed region in each condition in panel A is shown at a higher magnification beneath the corresponding section. SC, spinal cord; Ceb, cerebellum. Note that adjacent sections in each group were used for staining against CD68 and phospho-NFκB p65. Scale bars represent 500 and 50 μm for the spinal cord and 1 mm and 20 μm for the cerebellum at low-magnification and high magnification, respectively. (**B**-**E**) Statistical analysis of staining intensity for CD68 (A and B) and phosphor-NFκB p65 (pNFκB, D and E) in the spinal cord (B and D) and cerebellum (C and E), respectively. Data represent median ± range; Kruscal-Wallis test (non-parametric). ns, not significant. n = 4 and 8 mice for controls (Control: PBS>PTX; ETX: PBS>ETX-Hi) and EAE groups (PTX-EAE: MOG>PTX; ETX-EAE: MOG>ETX-Hi), respectively.

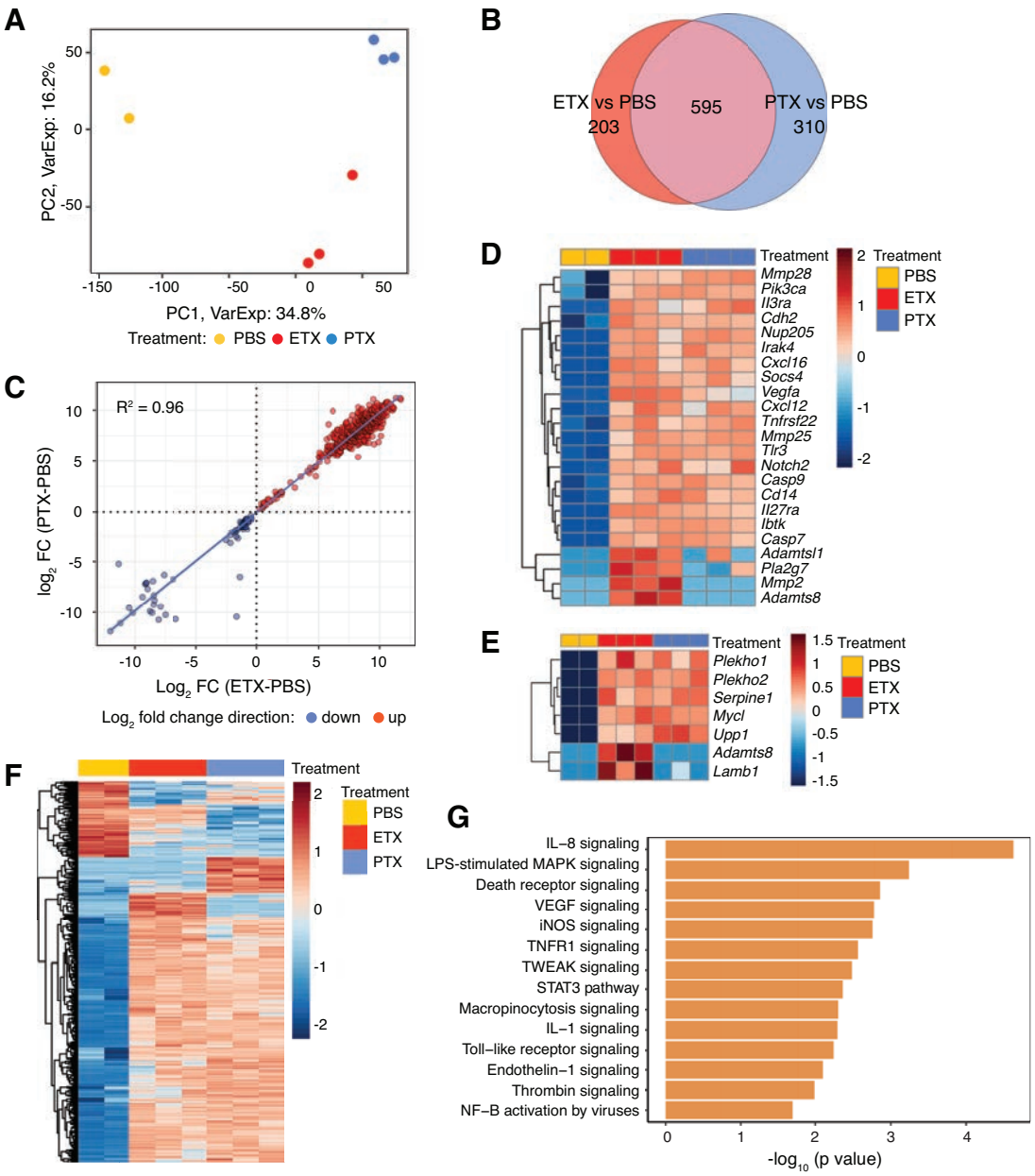

Figure 8. Transcriptome analysis of ETX and PTX treated CNS endothelial cells from spinal cord.

(**A**) Principal-component (PC) analysis of RNA-seq data, based on the top 1000 most variable genes. Each symbol represents a biological replicate, and each component is indicated with the amount of variation that it explains. n = 3 mice for PTX and ETX treatment and n = 2 mice for PBS treatment. (**B**) Venn diagram showing extent of overlap between genes differentially expressed

in ETX or PTX treated samples relative to control (PBS). (**C**) Correlation analysis of log_2 fold-changes between genes that change in both ETX and PTX displayed as a scatterplot, $R^2 = 0.96$. (**D**) Heat map of DEGs of interest relevant to immune privilege (FDR < 0.10) in ETX or PTX. (**E**) Heat map of DEGs induced by ETX and/or PTX reported by Munji (101) in a BBB dysfunction module. (**F**) Heat map of all DEGs induced by ETX and/or PTX relative to PBS control. (**G**) Selected pathways predicted to be activated in ETX treated cells by Ingenuity Pathway Analysis ($p < 0.05$ and z-score >= 1) based on the differentially expressed genes compared to PBS cells.

References

1. Dawson J. The Histology of Disseminated Sclerosis. *Transactions of the Royal Society of Edinburgh* 1916:517-740.
2. Lassmann H. Multiple Sclerosis Pathology. *Cold Spring Harb Perspect Med.* 2018;8(3).
3. Absinta M, Nair G, Sati P, Cortese IC, Filippi M, and Reich DS. Direct MRI detection of impending plaque development in multiple sclerosis. *Neurol Neuroimmunol Neuroinflamm.* 2015;2(5):e145.
4. Barnett MH, and Prineas JW. Relapsing and remitting multiple sclerosis: pathology of the newly forming lesion. *Ann Neurol.* 2004;55(4):458-68.
5. Marrie RA. Environmental risk factors in multiple sclerosis aetiology. *Lancet Neurol.* 2004;3(12):709-18.
6. Thompson AJ, Baranzini SE, Geurts J, Hemmer B, and Ciccarelli O. Multiple sclerosis. *Lancet.* 2018;391(10130):1622-36.
7. Miyauchi E, Shimokawa C, Steimle A, Desai MS, and Ohno H. The impact of the gut microbiome on extra-intestinal autoimmune diseases. *Nat Rev Immunol.* 2022.
8. Jangi S, Gandhi R, Cox LM, Li N, von Glehn F, Yan R, et al. Alterations of the human gut microbiome in multiple sclerosis. *Nat Commun.* 2016;7:12015.
9. Berer K, Gerdes LA, Cekanaviciute E, Jia X, Xiao L, Xia Z, et al. Gut microbiota from multiple sclerosis patients enables spontaneous autoimmune encephalomyelitis in mice. *Proc Natl Acad Sci U S A.* 2017;114(40):10719-24.
10. Chen J, Chia N, Kalari KR, Yao JZ, Novotna M, Paz Soldan MM, et al. Multiple sclerosis patients have a distinct gut microbiota compared to healthy controls. *Sci Rep.* 2016;6:28484.
11. Cosorich I, Dalla-Costa G, Sorini C, Ferrarese R, Messina MJ, Dolpady J, et al. High frequency of intestinal TH17 cells correlates with microbiota alterations and disease activity in multiple sclerosis. *Sci Adv.* 2017;3(7):e1700492.
12. Cekanaviciute E, Yoo BB, Runia TF, Debelius JW, Singh S, Nelson CA, et al. Gut bacteria from multiple sclerosis patients modulate human T cells and exacerbate symptoms in mouse models. *Proc Natl Acad Sci U S A.* 2017;114(40):10713-8.
13. Ventura RE, Iizumi T, Battaglia T, Liu M, Perez-Perez GI, Herbert J, et al. Gut microbiome of treatment-naive MS patients of different ethnicities early in disease course. *Sci Rep.* 2019;9(1):16396.
14. Mirza A, Forbes JD, Zhu F, Bernstein CN, Van Domselaar G, Graham M, et al. The multiple sclerosis gut microbiota: A systematic review. *Mult Scler Relat Disord.* 2020;37:101427.
15. Cantoni C, Lin Q, Dorsett Y, Ghezzi L, Liu Z, Pan Y, et al. Alterations of host-gut microbiome interactions in multiple sclerosis. *EBioMedicine.* 2022;76:103798.
16. Ghezzi L, Cantoni C, Pinget GV, Zhou Y, and Piccio L. Targeting the gut to treat multiple sclerosis. *J Clin Invest.* 2021;131(13).
17. Miyake S, Kim S, Suda W, Oshima K, Nakamura M, Matsuoka T, et al. Dysbiosis in the Gut Microbiota of Patients with Multiple Sclerosis, with a Striking Depletion of Species Belonging to Clostridia XIVa and IV Clusters. *PLoS One.* 2015;10(9):e0137429.

18. Mirza AI, Zhu F, Knox N, Forbes JD, Bonner C, Van Domselaar G, et al. The metabolic potential of the paediatric-onset multiple sclerosis gut microbiome. *Mult Scler Relat Disord.* 2022;63:103829.
19. i MCEasbue, and i MC. Gut microbiome of multiple sclerosis patients and paired household healthy controls reveal associations with disease risk and course. *Cell.* 2022;185(19):3467-86 e16.
20. Wekerle H. Nature, nurture, and microbes: The development of multiple sclerosis. *Acta Neurol Scand.* 2017;136 Suppl 201:22-5.
21. Rothhammer V, Borucki DM, Tjon EC, Takenaka MC, Chao CC, Ardura-Fabregat A, et al. Microglial control of astrocytes in response to microbial metabolites. *Nature.* 2018;557(7707):724-8.
22. Rothhammer V, Mascanfroni ID, Bunse L, Takenaka MC, Kenison JE, Mayo L, et al. Type I interferons and microbial metabolites of tryptophan modulate astrocyte activity and central nervous system inflammation via the aryl hydrocarbon receptor. *Nat Med.* 2016;22(6):586-97.
23. Miyauchi E, Kim SW, Suda W, Kawasumi M, Onawa S, Taguchi-Atarashi N, et al. Gut microorganisms act together to exacerbate inflammation in spinal cords. *Nature.* 2020;585(7823):102-6.
24. Schnell A, Huang L, Singer M, Singaraju A, Barilla RM, Regan BML, et al. Stem-like intestinal Th17 cells give rise to pathogenic effector T cells during autoimmunity. *Cell.* 2021;184(26):6281-98 e23.
25. Sanmarco LM, Wheeler MA, Gutierrez-Vazquez C, Polonio CM, Linnerbauer M, Pinho-Ribeiro FA, et al. Gut-licensed IFNgamma(+) NK cells drive LAMP1(+)TRAIL(+) anti-inflammatory astrocytes. *Nature.* 2021;590(7846):473-9.
26. Linden JR, Flores C, Schmidt EF, Uzal FA, Michel AO, Valenzuela M, et al. Clostridium perfringens epsilon toxin induces blood brain barrier permeability via caveolae-dependent transcytosis and requires expression of MAL. *PLoS Pathog.* 2019;15(11):e1008014.
27. Rood JI, Adams V, Lacey J, Lyras D, McClane BA, Melville SB, et al. Expansion of the Clostridium perfringens toxin-based typing scheme. *Anaerobe.* 2018;53:5-10.
28. Chen J, Ma M, Uzal FA, and McClane BA. Host cell-induced signaling causes Clostridium perfringens to upregulate production of toxins important for intestinal infections. *Gut Microbes.* 2014;5(1):96-107.
29. Chen J, and McClane BA. Role of the Agr-like quorum-sensing system in regulating toxin production by Clostridium perfringens type B strains CN1793 and CN1795. *Infect Immun.* 2012;80(9):3008-17.
30. Chen J, Rood JI, and McClane BA. Epsilon-toxin production by Clostridium perfringens type D strain CN3718 is dependent upon the agr operon but not the VirS/VirR two-component regulatory system. *mBio.* 2011;2(6).
31. Goldstein MR, Kruth SA, Bersenas AM, Holowaychuk MK, and Weese JS. Detection and characterization of Clostridium perfringens in the feces of healthy and diarrheic dogs. *Can J Vet Res.* 2012;76(3):161-5.

32. Regan SB, Anwar Z, Miraflor P, Williams LB, Shetty S, Sepulveda J, et al. Identification of epsilon toxin-producing Clostridium perfringens strains in American retail food. *Anaerobe.* 2018;54:124-7.
33. Anwar Z, Regan SB, and Linden J. Enrichment and Detection of Clostridium perfringens Toxinotypes in Retail Food Samples. *J Vis Exp.* 2019(152).
34. Lee CA, and Labbe R. Distribution of Enterotoxin- and Epsilon-Positive Clostridium perfringens Spores in U.S. Retail Spices. *J Food Prot.* 2018;81(3):394-9.
35. Madden RH, Buller H, and Mc DD. Clostridium perfringens as an Indicator of Hygienic Quality of Depurated Shellfish. *J Food Prot.* 1986;49(1):33-6.
36. Davies CM, Long JA, Donald M, and Ashbolt NJ. Survival of fecal microorganisms in marine and freshwater sediments. *Appl Environ Microbiol.* 1995;61(5):1888-96.
37. Miller WA, Miller MA, Gardner IA, Atwill ER, Byrne BA, Jang S, et al. Salmonella spp., Vibrio spp., Clostridium perfringens, and Plesiomonas shigelloides in marine and freshwater invertebrates from coastal California ecosystems. *Microb Ecol.* 2006;52(2):198-206.
38. Skanavis C, and Yanko WA. Clostridium perfringens as a potential indicator for the presence of sewage solids in marine sediments. *Mar Pollut Bull.* 2001;42(1):31-5.
39. Wade TJ, Sams E, Brenner KP, Haugland R, Chern E, Beach M, et al. Rapidly measured indicators of recreational water quality and swimming-associated illness at marine beaches: a prospective cohort study. *Environ Health.* 2010;9:66.
40. Li J, Sayeed S, and McClane BA. Prevalence of enterotoxigenic Clostridium perfringens Isolates in Pittsburgh (Pennsylvania) area soils and home kitchens. *Appl Environ Microbiol.* 2007;73(22):7218-24.
41. Drean P, McAuley CM, Moore SC, Fegan N, and Fox EM. Characterization of the spore-forming Bacillus cereus sensu lato group and Clostridium perfringens bacteria isolated from the Australian dairy farm environment. *BMC Microbiol.* 2015;15:38.
42. Strong DH, Canada JC, and Griffiths BB. Incidence of Clostridium perfringens in American foods. *Appl Microbiol.* 1963;11:42-4.
43. Wen Q, and McClane BA. Detection of enterotoxigenic Clostridium perfringens type A isolates in American retail foods. *Appl Environ Microbiol.* 2004;70(5):2685-91.
44. Talukdar PK, Udompijitkul P, Hossain A, and Sarker MR. Inactivation Strategies for Clostridium perfringens Spores and Vegetative Cells. *Appl Environ Microbiol.* 2017;83(1).
45. Talukdar PK, Olguin-Araneda V, Alnoman M, Paredes-Sabja D, and Sarker MR. Updates on the sporulation process in Clostridium species. *Res Microbiol.* 2015;166(4):225-35.
46. Hatheway CL. Toxigenic clostridia. *Clin Microbiol Rev.* 1990;3(1):66-98.
47. Hildebrand F, Nguyen TL, Brinkman B, Yunta RG, Cauwe B, Vandenabeele P, et al. Inflammation-associated enterotypes, host genotype, cage and inter-individual effects drive gut microbiota variation in common laboratory mice. *Genome Biol.* 2013;14(1):R4.
48. Bokori-Brown M, Savva CG, Fernandes da Costa SP, Naylor CE, Basak AK, and Titball RW. Molecular basis of toxicity of Clostridium perfringens epsilon toxin. *FEBS J.* 2011;278(23):4589-601.
49. Savva CG, Clark AR, Naylor CE, Popoff MR, Moss DS, Basak AK, et al. The pore structure of Clostridium perfringens epsilon toxin. *Nat Commun.* 2019;10(1):2641.
50. Popoff MR. Epsilon toxin: a fascinating pore-forming toxin. *FEBS J.* 2011;278(23):4602-15.

51. Freedman JC, Li J, Uzal FA, and McClane BA. Proteolytic processing and activation of Clostridium perfringens epsilon toxin by caprine small intestinal contents. *mBio.* 2014;5(5):e01994-14.
52. Harkness JM, Li J, and McClane BA. Identification of a lambda toxin-negative Clostridium perfringens strain that processes and activates epsilon prototoxin intracellularly. *Anaerobe.* 2012;18(5):546-52.
53. Goldstein J, Morris WE, Loidl CF, Tironi-Farinati C, McClane BA, Uzal FA, et al. Clostridium perfringens epsilon toxin increases the small intestinal permeability in mice and rats. *PLoS One.* 2009;4(9):e7065.
54. Rumah KR, Ma Y, Linden JR, Oo ML, Anrather J, Schaeren-Wiemers N, et al. The Myelin and Lymphocyte Protein MAL Is Required for Binding and Activity of Clostridium perfringens epsilon-Toxin. *PLoS Pathog.* 2015;11(5):e1004896.
55. Linden JR, Ma Y, Zhao B, Harris JM, Rumah KR, Schaeren-Wiemers N, et al. Clostridium perfringens Epsilon Toxin Causes Selective Death of Mature Oligodendrocytes and Central Nervous System Demyelination. *mBio.* 2015;6(3):e02513.
56. Adler D, Linden JR, Shetty SV, Ma Y, Bokori-Brown M, Titball RW, et al. Clostridium perfringens Epsilon Toxin Compromises the Blood-Brain Barrier in a Humanized Zebrafish Model. *iScience.* 2019;15:39-54.
57. Rumah KR, Linden J, Fischetti VA, and Vartanian T. Isolation of Clostridium perfringens type B in an individual at first clinical presentation of multiple sclerosis provides clues for environmental triggers of the disease. *PLoS One.* 2013;8(10):e76359.
58. Blanch M, Dorca-Arevalo J, Not A, Cases M, Gomez de Aranda I, Martinez-Yelamos A, et al. The Cytotoxicity of Epsilon Toxin from Clostridium perfringens on Lymphocytes Is Mediated by MAL Protein Expression. *Mol Cell Biol.* 2018;38(19).
59. Robertson SL, Li J, Uzal FA, and McClane BA. Evidence for a prepore stage in the action of Clostridium perfringens epsilon toxin. *PLoS One.* 2011;6(7):e22053.
60. Knapp O, Maier E, Waltenberger E, Mazuet C, Benz R, and Popoff MR. Residues involved in the pore-forming activity of the Clostridium perfringens iota toxin. *Cell Microbiol.* 2015;17(2):288-302.
61. Miyata S, Minami J, Tamai E, Matsushita O, Shimamoto S, and Okabe A. Clostridium perfringens epsilon-toxin forms a heptameric pore within the detergent-insoluble microdomains of Madin-Darby canine kidney cells and rat synaptosomes. *J Biol Chem.* 2002;277(42):39463-8.
62. Mander KA, and Finnie JW. Loss of Endothelial Barrier Antigen Immunoreactivity in Rat Retinal Microvessels is Correlated with Clostridium perfringens Type D Epsilon Toxin-induced Damage to the Blood-Retinal Barrier. *J Comp Pathol.* 2018;158:51-5.
63. Zhu C, Ghabriel MN, Blumbergs PC, Reilly PL, Manavis J, Youssef J, et al. Clostridium perfringens prototoxin-induced alteration of endothelial barrier antigen (EBA) immunoreactivity at the blood-brain barrier (BBB). *Exp Neurol.* 2001;169(1):72-82.
64. Finnie JW, and Hajduk P. An immunohistochemical study of plasma albumin extravasation in the brain of mice after the administration of Clostridium perfringens type D epsilon toxin. *Aust Vet J.* 1992;69(10):261-2.

65. Polman CH, Reingold SC, Banwell B, Clanet M, Cohen JA, Filippi M, et al. Diagnostic criteria for multiple sclerosis: 2010 revisions to the McDonald criteria. *Ann Neurol.* 2011;69(2):292-302.
66. Carman RJ, Sayeed S, Li J, Genheimer CW, Hiltonsmith MF, Wilkins TD, et al. Clostridium perfringens toxin genotypes in the feces of healthy North Americans. *Anaerobe.* 2008;14(2):102-8.
67. Li J, Sayeed S, Robertson S, Chen J, and McClane BA. Sialidases affect the host cell adherence and epsilon toxin-induced cytotoxicity of Clostridium perfringens type D strain CN3718. *PLoS Pathog.* 2011;7(12):e1002429.
68. Allaband C, McDonald D, Vazquez-Baeza Y, Minich JJ, Tripathi A, Brenner DA, et al. Microbiome 101: Studying, Analyzing, and Interpreting Gut Microbiome Data for Clinicians. *Clin Gastroenterol Hepatol.* 2019;17(2):218-30.
69. Eckburg PB, Bik EM, Bernstein CN, Purdom E, Dethlefsen L, Sargent M, et al. Diversity of the human intestinal microbial flora. *Science.* 2005;308(5728):1635-8.
70. Hevia A, Delgado S, Margolles A, and Sanchez B. Application of density gradient for the isolation of the fecal microbial stool component and the potential use thereof. *Sci Rep.* 2015;5:16807.
71. Wagley S, Bokori-Brown M, Morcrette H, Malaspina A, D'Arcy C, Gnanapavan S, et al. Evidence of Clostridium perfringens epsilon toxin associated with multiple sclerosis. *Mult Scler.* 2019;25(5):653-60.
72. Livak KJ, and Schmittgen TD. Analysis of relative gene expression data using real-time quantitative PCR and the 2(-Delta Delta C(T)) Method. *Methods.* 2001;25(4):402-8.
73. Popoff MR. Clostridial pore-forming toxins: powerful virulence factors. *Anaerobe.* 2014;30:220-38.
74. Nagpal R, Ogata K, Tsuji H, Matsuda K, Takahashi T, Nomoto K, et al. Sensitive quantification of Clostridium perfringens in human feces by quantitative real-time PCR targeting alpha-toxin and enterotoxin genes. *BMC Microbiol.* 2015;15:219.
75. Hughes ML, Poon R, Adams V, Sayeed S, Saputo J, Uzal FA, et al. Epsilon-toxin plasmids of Clostridium perfringens type D are conjugative. *J Bacteriol.* 2007;189(21):7531-8.
76. Li J, Adams V, Bannam TL, Miyamoto K, Garcia JP, Uzal FA, et al. Toxin plasmids of Clostridium perfringens. *Microbiol Mol Biol Rev.* 2013;77(2):208-33.
77. Revitt-Mills SA, Watts TD, Lyras D, Adams V, and Rood JI. The ever-expanding tcp conjugation locus of pCW3 from Clostridium perfringens. *Plasmid.* 2021;113:102516.
78. Adams V, Watts TD, Bulach DM, Lyras D, and Rood JI. Plasmid partitioning systems of conjugative plasmids from Clostridium perfringens. *Plasmid.* 2015;80:90-6.
79. Murrell TG, O'Donoghue PJ, and Ellis T. A review of the sheep-multiple sclerosis connection. *Med Hypotheses.* 1986;19(1):27-39.
80. Miyamoto K, Li J, Sayeed S, Akimoto S, and McClane BA. Sequencing and diversity analyses reveal extensive similarities between some epsilon-toxin-encoding plasmids and the pCPF5603 Clostridium perfringens enterotoxin plasmid. *J Bacteriol.* 2008;190(21):7178-88.
81. Linden JR, Telesford K, Shetty S, Winokour P, Haigh S, Cahir-McFarland E, et al. A Novel Panel of Rabbit Monoclonal Antibodies and Their Diverse Applications Including Inhibition of Clostridium perfringens Epsilon Toxin Oligomerization. *Antibodies (Basel).* 2018;7(4).

82. Waturuocha UW, Krishna MS, Malhotra V, Dixit NM, and Saini DK. A Low-Prevalence Single-Nucleotide Polymorphism in the Sensor Kinase PhoR in Mycobacterium tuberculosis Suppresses Its Autophosphatase Activity and Reduces Pathogenic Fitness: Implications in Evolutionary Selection. *Front Microbiol.* 2021;12:724482.
83. Weissman SJ, Moseley SL, Dykhuizen DE, and Sokurenko EV. Enterobacterial adhesins and the case for studying SNPs in bacteria. *Trends Microbiol.* 2003;11(3):115-7.
84. Mahamat Abdelrahim A, Radomski N, Delannoy S, Djellal S, Le Negrate M, Hadjab K, et al. Large-Scale Genomic Analyses and Toxinotyping of Clostridium perfringens Implicated in Foodborne Outbreaks in France. *Front Microbiol.* 2019;10:777.
85. Lacey JA, Allnutt TR, Vezina B, Van TTH, Stent T, Han X, et al. Whole genome analysis reveals the diversity and evolutionary relationships between necrotic enteritis-causing strains of Clostridium perfringens. *BMC Genomics.* 2018;19(1):379.
86. Sauna ZE, and Kimchi-Sarfaty C. Understanding the contribution of synonymous mutations to human disease. *Nat Rev Genet.* 2011;12(10):683-91.
87. Wekerle HaL, H. *McAlpine's Multiple Sclerosis*. 2006:491-555.
88. Walker LS, and Abbas AK. The enemy within: keeping self-reactive T cells at bay in the periphery. *Nat Rev Immunol.* 2002;2(1):11-9.
89. Carson MJ, Doose JM, Melchior B, Schmid CD, and Ploix CC. CNS immune privilege: hiding in plain sight. *Immunol Rev.* 2006;213:48-65.
90. Engelhardt B, Vajkoczy P, and Weller RO. The movers and shapers in immune privilege of the CNS. *Nat Immunol.* 2017;18(2):123-31.
91. Laaker C, Hsu M, Fabry Z, Miller SD, and Karpus WJ. Experimental Autoimmune Encephalomyelitis in the Mouse. *Curr Protoc.* 2021;1(12):e300.
92. Richard JF, Roy M, Audoy-Remus J, Tremblay P, and Vallieres L. Crawling phagocytes recruited in the brain vasculature after pertussis toxin exposure through IL6, ICAM1 and ITGalphaM. *Brain Pathol.* 2011;21(6):661-71.
93. Schellenberg AE, Buist R, Del Bigio MR, Toft-Hansen H, Khorooshi R, Owens T, et al. Blood-brain barrier disruption in CCL2 transgenic mice during pertussis toxin-induced brain inflammation. *Fluids Barriers CNS.* 2012;9(1):10.
94. Bettelli E, Pagany M, Weiner HL, Linington C, Sobel RA, and Kuchroo VK. Myelin oligodendrocyte glycoprotein-specific T cell receptor transgenic mice develop spontaneous autoimmune optic neuritis. *J Exp Med.* 2003;197(9):1073-81.
95. Millan J, and Alonso MA. MAL, a novel integral membrane protein of human T lymphocytes, associates with glycosylphosphatidylinositol-anchored proteins and Src-like tyrosine kinases. *Eur J Immunol.* 1998;28(11):3675-84.
96. Pape KA, Kearney ER, Khoruts A, Mondino A, Merica R, Chen ZM, et al. Use of adoptive transfer of T-cell-antigen-receptor-transgenic T cell for the study of T-cell activation in vivo. *Immunol Rev.* 1997;156:67-78.
97. Moon JJ, Chu HH, Hataye J, Pagan AJ, Pepper M, McLachlan JB, et al. Tracking epitope-specific T cells. *Nat Protoc.* 2009;4(4):565-81.
98. Ronchi F, Basso C, Preite S, Reboldi A, Baumjohann D, Perlini L, et al. Experimental priming of encephalitogenic Th1/Th17 cells requires pertussis toxin-driven IL-1beta production by myeloid cells. *Nat Commun.* 2016;7:11541.

99. Pulido RS, Munji RN, Chan TC, Quirk CR, Weiner GA, Weger BD, et al. Neuronal Activity Regulates Blood-Brain Barrier Efflux Transport through Endothelial Circadian Genes. *Neuron.* 2020;108(5):937-52 e7.
100. Law CW, Chen Y, Shi W, and Smyth GK. voom: Precision weights unlock linear model analysis tools for RNA-seq read counts. *Genome Biol.* 2014;15(2):R29.
101. Munji RN, Soung AL, Weiner GA, Sohet F, Semple BD, Trivedi A, et al. Profiling the mouse brain endothelial transcriptome in health and disease models reveals a core blood-brain barrier dysfunction module. *Nat Neurosci.* 2019;22(11):1892-902.
102. Cree BA, Spencer CM, Varrin-Doyer M, Baranzini SE, and Zamvil SS. Gut microbiome analysis in neuromyelitis optica reveals overabundance of Clostridium perfringens. *Ann Neurol.* 2016;80(3):443-7.
103. Zamvil SS, Spencer CM, Baranzini SE, and Cree BAC. The Gut Microbiome in Neuromyelitis Optica. *Neurotherapeutics.* 2018;15(1):92-101.
104. Garcia JP, Adams V, Beingesser J, Hughes ML, Poon R, Lyras D, et al. Epsilon toxin is essential for the virulence of Clostridium perfringens type D infection in sheep, goats, and mice. *Infect Immun.* 2013;81(7):2405-14.
105. Songer JG. Clostridial enteric diseases of domestic animals. *Clin Microbiol Rev.* 1996;9(2):216-34.
106. Uzal FAG, F.; Finnie, J.W.; Garcia, J.P. . In: Uzal FAS, J.G.; Prescott, J.F.; Popoff, M.R. ed. *Clostridial Diseases of Animals*. Ames, IA, USA: Wiley-Blackwell; 2016:157-72.
107. Finnie JW. Neurological disorders produced by Clostridium perfringens type D epsilon toxin. *Anaerobe.* 2004;10(2):145-50.
108. Bjornevik K, Cortese M, Healy BC, Kuhle J, Mina MJ, Leng Y, et al. Longitudinal analysis reveals high prevalence of Epstein-Barr virus associated with multiple sclerosis. *Science.* 2022;375(6578):296-301.
109. Lanz TV, Brewer RC, Ho PP, Moon JS, Jude KM, Fernandez D, et al. Clonally Expanded B Cells in Multiple Sclerosis Bind EBV EBNA1 and GlialCAM. *Nature.* 2022.
110. Winter JR, Taylor GS, Thomas OG, Jackson C, Lewis JEA, and Stagg HR. Predictors of Epstein-Barr virus serostatus in young people in England. *BMC Infect Dis.* 2019;19(1):1007.
111. Horwitz RI, Hayes-Conroy A, Singer BH, Cullen MR, Badal K, and Sim I. Falling down the biological rabbit hole: Epstein-Barr virus, biography, and multiple sclerosis. *J Clin Invest.* 2022;132(17).
112. Nathan C. Nonresolving inflammation redux. *Immunity.* 2022;55(4):592-605.